International Journal of Solids and Structures 283 (2023) 112475

Contents lists available at ScienceDirect

International Journal of Solids and Structures

journal homepage: www.elsevier.com/locate/ijsolstr

Modelling the Mullins effect and the magnetic-dependent nonlinear viscoelasticity of isotropic soft magnetorheological elastomers

Yan Li [a], Bochao Wang [a,c,*], Xinglong Gong [a,b,*]

[a] CAS Key Laboratory of Mechanical Behaviour and Design of Materials, Department of Modern Mechanics, University of Science and Technology of China, Hefei, 230027, China
[b] State Key Laboratory of Fire Science University of Science and Technology of China (USTC), Hefei, 230026, China
[c] Anhui Weiwei Rubber Part Group Co. Ltd., Tongcheng, 231460, China

ARTICLE INFO

Keywords:
Isotropic soft magnetorheological elastomers
Constitutive modelling
Magnetic-dependent Mullins effect
Magnetic-dependent nonlinear viscoelasticity
Numerical simulation

ABSTRACT

Soft magnetorheological elastomers (s-MRE) are a smart material mainly prepared by filling soft magnetic particles into an elastomeric matrix. Under the influence of a magnetic field, the mechanical properties of the material can be changed rapidly and reversibly, offering a broad application prospect in vibration control, magnetic actuation and other areas. Due to the embedding of the magnetic particles, an obvious stress-softening phenomenon (Mullins effect) and magnetic-dependent nonlinear viscoelasticity are exhibited for the s-MRE. Recent theoretical studies mainly focused on modelling the magnetostriction and the magnetic-dependent hyperelastic behaviour of s-MRE, while less attention is paid to modelling its magnetic-dependent inelastic behaviour. However, the stress-softening and the magnetic-dependent nonlinear viscoelastic behaviour play a vital role in the application of s-MRE. In order to predict the magneto-mechanical coupling behaviour of s-MRE accurately, a constitutive model which incorporates the Mullins effect and the magnetic-dependent nonlinear viscoelastic behaviour of isotropic s-MRE is proposed. The comparison between the simulation and experimental results indicates that the residual strain, magnetic-dependent Mullins effect and nonlinear viscoelastic behaviour of isotropic s-MRE are well depicted by the model. The developed model provides a theoretical basis for the design and application of isotropic s-MRE in vibration control, magnetic drive and other fields and promotes its potential application.

1. Introduction

Soft magnetorheological elastomers (s-MRE) are a smart material fabricated by embedding soft magnetic particles (such as carbonyl iron and Fe_3O_4) into the elastomeric matrix. Under a magnetic field, the mechanical properties such as the modulus and damping of s-MRE can be changed rapidly and reversibly (Jolly et al., 1996; Abramchuk et al., 2007). By utilizing the modulus magnetic stiffening effect, applications of s-MRE in the areas of vibration control (Lin et al., 2023; Fu et al., 2016; Gao et al., 2021), acoustic metamaterial (Chen et al., 2022) and bionic design (Hong et al., 2022) have been explored. Moreover, due to the soft nature of the elastomeric matrix and the large magnetic permeability of s-MRE, traction is induced at the s-MRE-air interface if a magnetic field is applied. Due to the magnetic-induced traction, an obvious magnetostriction of the s-MRE is exhibited. Studies investigating the magnetostriction mechanism of s-MRE in cardiovascular surgery (Hooshiar et al., 2021), haptic displays (Psarra et al., 2017, 2019) and tissue engineering (Moreno-Mateos et al., 2022) have been conducted.

To promote the application of s-MRE, a constitutive model which can accurately depict the magneto-mechanical coupling behaviour of s-MRE is needed. As a special filler rubber, a pronounced stress-softening associated with residual strain and nonlinear viscoelasticity displays for the s-MRE. Furthermore, the interaction between magnetic particles and the polymer matrix under a magnetic field leads to a magnetic-dependence on the mechanical behaviour of s-MRE. Significant effort has been made to model the magneto-mechanical coupling behaviour of s-MRE. Primarily, Jolly et al. (1996) utilized the magnetic dipole theory to simulate the quasi-static magnetic-dependent mechanical behaviour of s-MRE. Subsequently, Zhu et al. (2006) extended the model by considering the influence of adjacent chains. Wang and Kari (2019a,b) and Zhu et al. (2020) incorporated a fractional derivative element to predict the viscoelastic behaviour of s-MRE under an infinitesimal

* Corresponding authors at: CAS Key Laboratory of Mechanical Behaviour and Design of Materials, Department of Modern Mechanics, University of Science and Technology of China, Hefei, 230027, China.
E-mail addresses: wangboc@ustc.edu.cn (B. Wang), gongxl@ustc.edu.cn (X. Gong).

https://doi.org/10.1016/j.ijsolstr.2023.112475
Received 23 April 2023; Received in revised form 5 August 2023; Accepted 29 August 2023
Available online 7 September 2023

strain assumption. However, due to the soft nature of s-MRE, a finite strain range should be applied to depict its magneto-mechanical coupling behaviour. Pioneering work to develop a theoretical framework for MRE based on continuum mechanics and electrodynamics was performed by Brown (1966) and Dorfmann and Ogden (2014). Subsequently, the homogenization method was incorporated into the model by Galipeau and Castaneda (2013), Zabihyan et al. (2020), Lefèvre et al. (2017) and Mukherjee et al. (2020). Bustamante (2010) and Shariff et al. (2017) extended the model to anisotropic case. Psarra et al. (2017, 2019) and Rambausek and Danas (2020) proposed a fully coupled magneto-mechanical finite element computational platform to simulate the behaviour of an isotropic s-MRE film rested on a non-magnetic elastomer. Based on these studies, the magnetostriction behaviour of isotropic s-MRE under a relatively slow magnetic loading rate can be predicted with accuracy. Unlike the work by Psarra et al. (2017, 2019) and Rambausek and Danas (2020); where the Helmholtz free energy is additively decoupled into hyperelastic and pure magnetic parts, Saxena et al. (2013), Haldar et al. (2016) and Haldar (2021) proposed a multiplicatively-typed free energy function to depict the modulus magnetic stiffening effect and viscoelastic behaviour of isotropic s-MRE. Rambausek et al. (2022) and Lucarini et al. (2022a) extended the viscoelastic model by incorporating the microstructurally guided homogenization method. Although the viscoelastic models proposed by Saxena et al. (2013), Haldar et al. (2016) and Haldar (2021) fulfil the dissipation inequality, the viscosity is assumed to be a process-independent value. However, as a special filler rubber, a typical nonlinear viscoelastic behaviour is exhibited for s-MRE. For instance, experimental studies by Blom and Kari (2005), Lejon and Kari (2013) and Bastola and Hossain (2020) indicated that the dynamic modulus of isotropic s-MRE decreases with increasing strain amplitude. Relaxation test by Qi et al. (2017) and Nam et al. (2021, 2022) demonstrated that a longer relaxation time is needed for the isotropic s-MRE if a larger magnetic field is applied. Therefore, a more elaborated constitutive model with a process-dependent viscosity evolution law is needed to depict the magnetic-dependent nonlinear viscoelastic behaviour of isotropic s-MRE.

Turning away the attention from the theoretical study of MRE to regular filler rubber for a while, the Mullins effect of filler rubber is well known. In particular, a typical and irreversible stress-softening effect (Harwood et al., 1965) displays for the filler-embedded rubber whenever the load increases beyond the maximum value in loading history. Besides the Mullins effect, other inelastic effects arise under loading and unloading. For example, the stress–strain curves for filler rubber are essentially rate-dependent (Amin et al., 2006; Moreno et al., 2021). Additionally, a residual strain (Dorfmann and Ogden, 2004), where the tested sample does not return to its original shape after unloading, is also encountered. Constitutive models based on the microscopic damage mechanism to explain the Mullins effect can be found in Govindjee and Simo (1991), Kilian et al. (1994) and Marckmann et al. (2002). The review paper by Diani et al. (2009) attributed the Mullins effect to three possible microscopic mechanisms, i.e., the changes in the filler-matrix relation, filler network and the damage in the rubber matrix. Contrary to the microscopically guided model, Ogden and Roxburgh (1999) proposed a pseudo-elastic phenomenological model and Simo (1987) proposed a damage model to describe the stress-softening behaviour of filler rubber. Dorfmann and Ogden (2004) extended the pseudo-elastic model by introducing an additional internal variable to reflect the residual strain. Regarding the modelling of the rate dependency for polymer, numerous studies are in the scope of continuum mechanics. Some representative studies related to this manuscript are pointed out below for brevity. Reese and Govindjee (1998) proposed the finite strain nonlinear viscoelastic theory. Primarily, a simple evolution equation where a linear relation between the inelastic strain rate and the overstress is assumed. However, such a linear assumption is not consistent with test results. Subsequently, Bergström and Boyce (1998), Hoefer and Lion (2009) and Amin et al. (2006) proposed nonlinear process-dependent viscoelastic models. The basic assumption is that other constitutive quantities, such as the viscous strain and the total strain, influence the overstress-dependence of the inelastic strain rate. Theoretically, the above-mentioned inelastic effects (Mullins effect, nonlinear viscoelasticity) of filler rubber are often studied separately. However, in practice, these inelastic behaviours occur simultaneously in a coupled manner. The situation is more complicated for isotropic s-MRE since there is an obvious magnetic-dependence of the mechanical behaviour for isotropic s-MRE besides the Mullins effect and the nonlinear viscoelasticity.

To promote the application of mre, a constitutive model incorporating the magnetic-dependent Mullins effect and the nonlinear viscoelasticity is needed to describe complex inelastic behaviours of s-MRE. For instance, the more accurate the constitutive model is in predicting the stress–strain relationship for the s-MRE, the more effective the controller will be in attenuation the vibration for the application of MRE in vibration control area. If the influence of the Mullins effect is not taken into account, an overestimation of the force response for MRE-based vibration devices during operation encounters. Subsequently, due to the deviation between the actual and predicted response, the vibration control effect may deteriorate to a large extent.

Based on the research status of s-MRE constitutive modelling mentioned above, a constitutive model which includes stress-softening, residual strain and magnetic-dependent nonlinear viscoelastic behaviour is proposed for the isotropic s-MRE. The organization of this paper is as follows. In Section 2, the fabrication process and the uniaxial tension experiments to characterize the magnetic-dependent Mullins effect and the stress relaxation of the isotropic s-MRE are introduced. In Section 3, the fundamentals of kinematics and magnetic field equations, along with the thermodynamic inequality for the model, are presented. Subsequently, the specific constitutive equations to describe the Mullins effect, residual strain and the nonlinear viscoelastic behaviour of the isotropic s-MRE are proposed in Section 4. Besides, the parameter identification process and model verification are conducted. Finally, the conclusions and outlook of this paper are summarized in Section 5. Regarding the numerical implementation algorithms corresponding to the model, details are shown in Appendix. Regarding the contribution of this work, firstly, the digital image correlation technology (DIC) and the magnetic excitation component are integrated into the dynamic mechanical analyzer to characterize the magneto-mechanical coupling behaviour of isotropic s-MRE. Secondly, a new constitutive model based on the experimental test results is established to depict the magnetic-dependent Mullins effect and nonlinear viscoelastic behaviour of isotropic s-MRE. The developed model can provide a theoretical basis for predicting the process and magnetic-dependent nonlinear mechanical behaviour of isotropic s-MRE, thereby facilitating designs of MRE-based devices.

2. Material fabrication and experimental characterization

In this section, the fabrication process, the experimental test setup, and the test results for the magnetic-dependent Mullins effect and stress relaxation of the isotropic s-MRE are presented.

2.1. Sample preparation and magnetic test results

To prepare isotropic s-MRE samples, firstly, carbonyl iron particles (CIPs, type CN, BASF, Germany diameter 7 μm on average), polydimethylsiloxane (PDMS) and cross-linking agent are mixed in a mass ratio of 140:60:3. The PDMS and cross-linking agent belong to SylgardTM 184 silicon elastomer kit, purchased from Dow Corning, United States. After mixing for 5 min, the mixture is put into a vacuum chamber under a pressure of 0.06 MPa to remove air bubbles. Afterwards, the mixture is poured into a rectangular mould with a thickness of 2 mm for curing. During the curing process, no magnetic

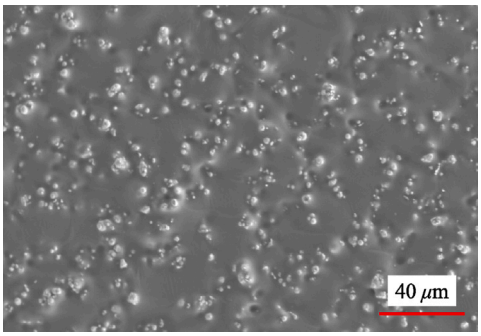

Fig. 1. Microscopic morphology of the isotropic s-MRE sample profile captured by a SEM.

field is applied, and the temperature is fixed at 100 °C. After curing for 30 min, the fabricated isotropic s-MRE is cut into test samples with a size of $2 \times 10 \times 45$ mm^3. The microscopic morphology of the fabricated isotropic s-MRE is obtained by a scan electron microscopy (SEM, Philips of Holland, model XL30 ESEM-TMP). As shown in Fig. 1, the CIPs are randomly distributed within the matrix, indicating the isotropy of the material.

The magnetization property of the isotropic s-MRE is tested by a magnetic measurement system (model MPMS3, Quantum Design, USA), and the results are shown in Fig. 2. Due to the magnetically soft nature of the carbonyl iron particles, the area enclosed by the magnetic hysteresis loop is very small. Furthermore, as shown in Fig. 2, the magnetization intensity of the isotropic s-MRE increases with increasing magnetic field strength until a magnetic saturation is reached. Moreover, by comparing the hysteresis curves in different directions, it can be seen that the sample is magnetic isotropy.

2.2. Magnetic-dependent Mullins effect and stress relaxation test results

A schematic diagram of the detailed experimental setup is shown in Fig. 3. The magnetic-dependent mechanical behaviour of the isotropic s-MRE is characterized by a series of uniaxial tensile tests using an Electro-Force 3200 Dynamic Mechanical Analyzer (DMA) from TA Instrument Inc. Two pairs of permanent magnets with a diameter of 60 mm are utilized to apply different magnetic (0.26 and 0.49 T) for the test sample, respectively. The magnetic field is measured by a Tesla meter with the sample inserted between the permanent magnets. The fluctuation of magnetic field on the interface between air and isotropic s-MRE does not exceed 20 mT, so the magnetic field is almost uniform when passing through the interface. A high-resolution CCD camera (MV-CA050-11UM, Hikvision, China) is used to record the deformation of the test sample and a digital image correction (DIC) technology (e.g., Landauer et al. (2019) and Li et al. (2022)) is applied to obtain the corresponding strain. Additionally, the displacement field of the sample in the 9×9 mm^2 region of interest with a tensile amplitude of 3.6 mm is shown in Fig. 4. From the displacement field contour plots shown in Fig. 4(b), it can be found that the displacements u_x and u_y vary linearly along the $x-$ and $y-$directions, demonstrating that a homogeneous deformation is achieved for the test sample.

During experimental testing, firstly, the magnetic-dependent Mullins effect and the viscoelastic behaviour of the isotropic s-MRE are tested separately to stimulate the constitutive modelling. Afterwards, triangular strain loading with consecutively increasing strain amplitudes under a relatively fast loading rate where the Mullins effect and the viscoelastic behaviour of the isotropic s-MRE occur in a coupled manner is conducted to validate the constitutive model. Furthermore, sinusoidal wave loading with different frequencies and strain amplitudes is used to further illustrate the predictive ability of the model for viscoelastic behaviour. Details regarding the model validation test will be introduced in Section 4. In addition, the selected strain amplitudes are pre-stated before the detailed experimental presentation. The initially selected displacement amplitudes are 2.0, 2.8, and 3.6 mm, corresponding to strain values of 10, 14, and 18%. The reason for choosing these three strain amplitudes is that in this strain range (less than 18%), the magneto-rheological effect of the isotropic s-MRE is obvious and stable. Some previous test results (e.g. Schubert and Harrison (2015) and Norouzi et al. (2016)) indicated that the magneto-rheological effect will be degraded if the strain is further increased. Since the work in this manuscript aims to guide the application of the isotropic s-MRE in the vibration control area that requires obvious and stable magneto-rheological effects, the three kinds of strain amplitude 10.0, 14.0 and 18.0% are selected. After applying loading, a slight slippage of the test sample between the two grips is encountered, and the strain detected by the DIC technology is a bit smaller than the original values where the corresponding values change into 9.0, 12.6 and 16.2%. For the following model development and parameter identification, the strain detected by the DIC technology is utilized directly.

To study the magnetic-dependent inelastic behaviours of the isotropic s-MRE, quasi-static tensile and stress relaxation tests are conducted. Specifically, a three-cycle triangular strain loading with consecutively increasing strain magnitudes (9.0, 12.6 and 16.2%) is applied to characterize the Mullins effect and the residual strain of the sample. The strain rate is set to 9.0×10^{-6} s^{-1} in the current tensile test to dismiss the rate dependency on the test result. Three magnetic fields of 0, 0.26 and 0.49 T are applied to reflect the influence of the magnetic field on the Mullins effect. The application of magnetic field results in the Maxwell force. To eliminate the influence of the Maxwell force on the subsequent test results, the positions of the mechanical grips as shown in Fig. 3 are adjusted prior to the main measurements to make sure that the internal stress caused by the Maxwell force is fully released. On the other hand, since the magnetic induced strain is at the order of 1% (0.49 T), the influence to the test result can be almost negligible. Besides the quasi-static tensile tests, stress relaxation tests under a strain rate of 4.5×10^{-2} s^{-1} with different strain amplitudes (9.0, 12.6 and 16.2%) and magnetic fields (0, 0.26 and 0.49 T) are conducted to characterize the magnetic-dependent viscoelastic behaviour of the isotropic s-MRE. To guarantee the reliability of the test results, the tests mentioned above are repeated three times, and the mean value is taken as the final data.

The quasi-static tensile and stress relaxation test results are shown in Figs. 5 and 6, respectively. The mechanical behaviour of the isotropic s-MRE exhibits an obvious magnetic-dependence. Specifically, for the quasi-static tensile test, the peak stress at 16.2% strain at 0 and 0.49 T are 0.239 and 0.260 MPa, respectively. In addition, it is worth noting that even when a very slow strain rate is applied in quasi-static testing, there is an energy dissipation, as demonstrated by the area enclosed for the stress–strain curve in Fig. 5. As reported by Li and Yang (2014), this effect may be caused by the microscopic damage of the material. In addition, in order to illustrate the coupling between the Mullins effect and the magnetic field, as well as the coupling between the viscoelasticity and the magnetic field, the experimental results obtained by the triangular loading with a faster strain rate are needed. Therefore, the test data by the triangular loading with a faster loading rate are displayed herein in Fig. 7 as well. As shown in Fig. 7, compared with the results in Fig. 5, a higher peak stress is encountered if a faster loading rate is applied.

3. Fundamentals of continuum mechanics and electromagnetics

Due to the soft nature of the elastomeric matrix and the magneto-mechanical coupling behaviour of isotropic s-MRE, continuum mechanics and electromagnetism theory are utilized to depict the magnetic-dependent mechanical behaviour of isotropic s-MRE. In this section, firstly, the fundamental continuum mechanics and magnetic equations

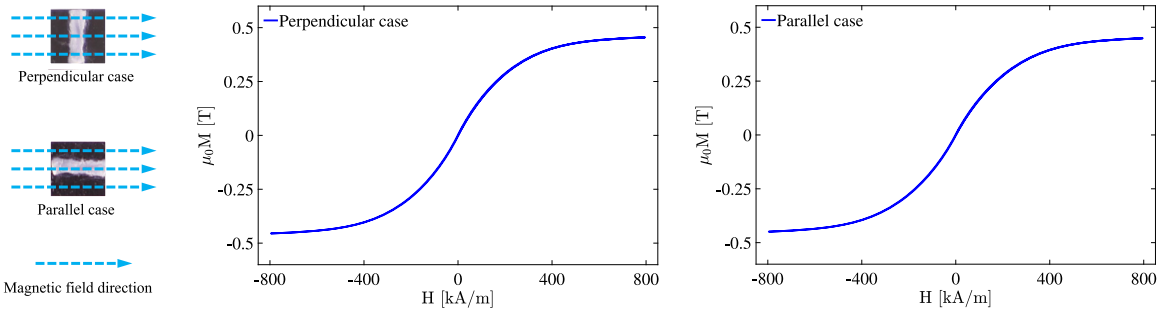

Fig. 2. Hysteresis curves in two directions for the isotropic s-MRE sample captured by the magnetic measurement system (the white mark is used to distinguish the position of the sample relative to the magnetic field).

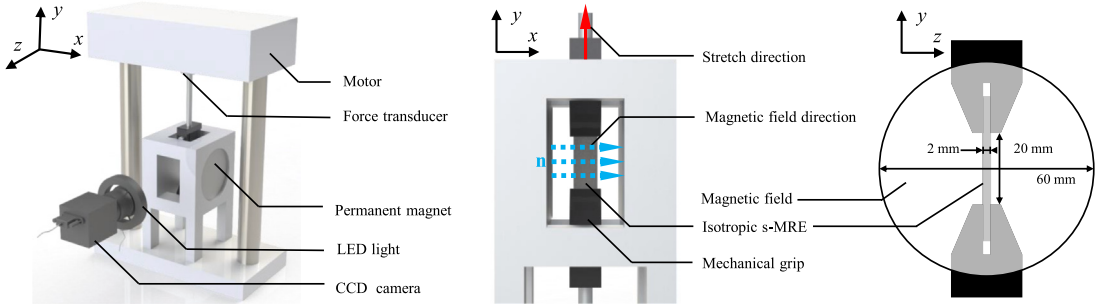

Fig. 3. Schematic diagrams of the DMA test system with external magnetic field generator and strain measuring system. Left: overall structure diagram of the test system. Middle: Local magnification diagram of the isotropic s-MRE sample under magnetic field and strain loading. Right: Comparison of magnetic field and sample size.

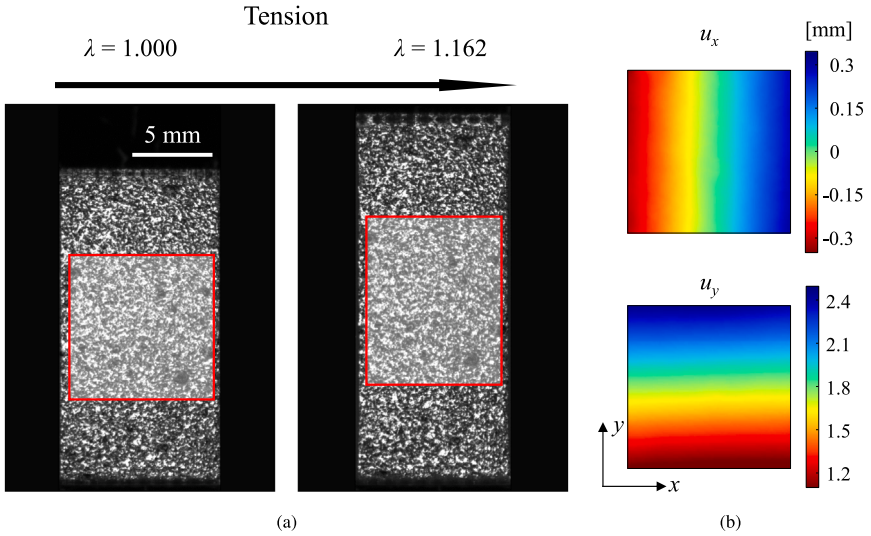

Fig. 4. The displacement results of the isotropic s-MRE sample in a $9 \times 9\,\text{mm}^2$ region of interest obtained by the DIC technology. (a) Region of interest before and after deformation. (b) Contour plots of displacements u_x and u_y.

are introduced. Afterwards, the stress and the magnetic flux density are obtained by the constitutive equation fulfilling the Clausius–Planck thermodynamic inequality. In this text, lowercase italics are applied for scalars and bold letters are applied for first- and second-order tensors. Unless stated, an overline denotes the volume-preserving part of strain tensors and a dot above a second-order tensor denotes the time derivative of the tensor, respectively.

3.1. Frame of kinematics

As shown in Fig. 8, the reference configuration without magnetic and mechanical loading is $\Omega_{\text{reference}}$. After loading, a typical material point with a position vector $\mathbf{X}$ deforms from $\Omega_{\text{reference}}$ to the current position $\mathbf{x}$ in Ω_{current}. The corresponding deformation gradient $\mathbf{F}$ is

$$\mathbf{F} = \text{Grad}\,\chi(\mathbf{X}, t), \tag{1}$$

where $\chi(\mathbf{X}, t)$ denotes the motion and t is time. Grad represents the gradient operator with respect to $\mathbf{X}$. The left and right Cauchy–Green strain tensors are $\mathbf{b} = \mathbf{F}\mathbf{F}^{\mathrm{T}}$ and $\mathbf{C} = \mathbf{F}^{\mathrm{T}}\mathbf{F}$, respectively. To ensure the future possible finite element implementation based on the modelling work, the isotropic s-MRE is assumed to be quasi-compressible. Consequently, the deformation gradient is multiplicatively decomposed into a volume-changing part $J = \det(\mathbf{F})$ and a volume-preserving part $\overline{\mathbf{F}} = J^{-1/3}\mathbf{F}$ (Simo, 1987). Furthermore, the theoretical path of the finite strain viscoelastic theory (e.g., Lubliner (1985) and Reese and

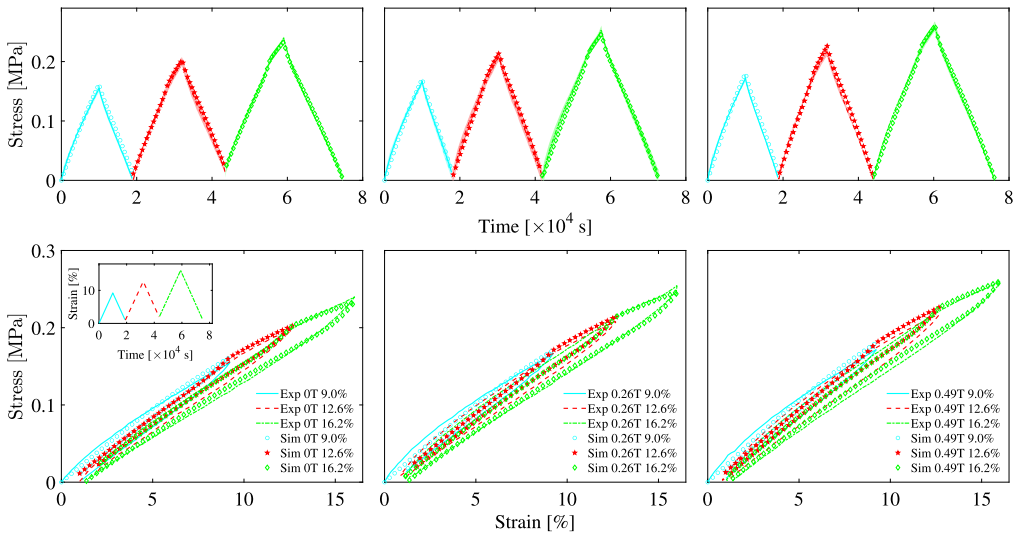

Fig. 5. Experimental (Exp) and simulation (Sim) results of the quasi-static loading tests (9.0×10^{-6} s^{-1}) under different magnetic fields (0, 0.26 and 0.49 T) with increasing strain magnitudes (9.0, 12.6 and 16.2%), where experimental scatter is shown in the light-coloured regions of the stress-time curves.

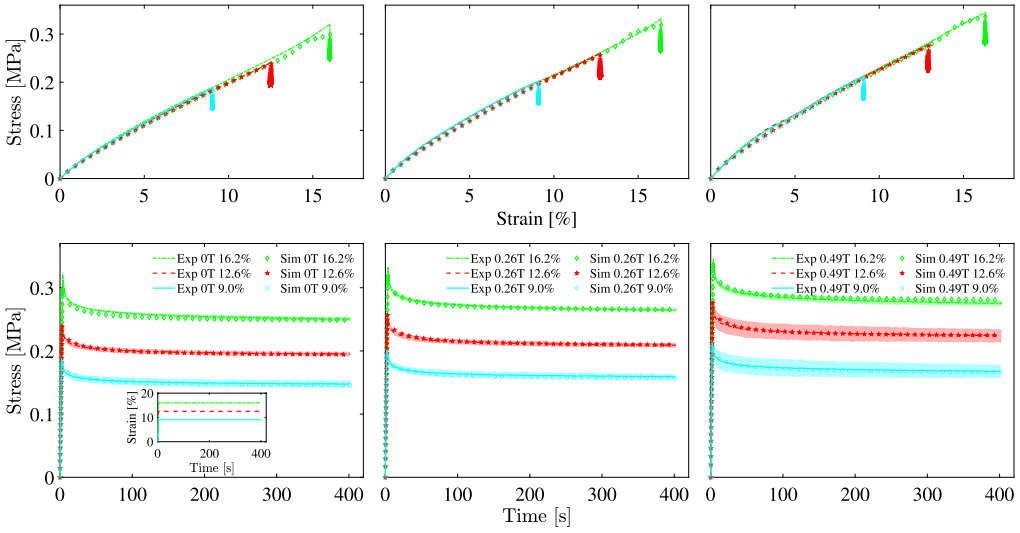

Fig. 6. Experimental (Exp) and simulation (Sim) results of stress relaxation tests under different magnetic fields (0, 0.26 and 0.49 T) and strain amplitudes (9.0, 12.6 and 16.2%), where experimental scatter is shown in the light-coloured regions of the stress-time curves.

Govindjee (1998)) is followed to depict the viscoelastic behaviour of the isotropic s-MRE. Subsequently, the unimodular deformation gradient $\overline{\mathbf{F}}$ is further multiplicatively decomposed into an elastic part $\overline{\mathbf{F}}^{\mathrm{e}}$ and a viscous part $\overline{\mathbf{F}}^{\mathrm{v}}$ in the form of

$$\overline{\mathbf{F}} = \overline{\mathbf{F}}^{\mathrm{e}}\overline{\mathbf{F}}^{\mathrm{v}}. \tag{2}$$

The corresponding unimodular elastic and viscous right Cauchy–Green tensors are $\overline{\mathbf{C}}^{\mathrm{e}} = \overline{\mathbf{F}}^{\mathrm{e}\mathrm{T}}\overline{\mathbf{F}}^{\mathrm{e}}$ and $\overline{\mathbf{C}}^{\mathrm{v}} = \overline{\mathbf{F}}^{\mathrm{v}\mathrm{T}}\overline{\mathbf{F}}^{\mathrm{v}}$, respectively. The symbol $\mathbf{S}$ in Fig. 8 denotes the second Piola–Kirchhoff stress in the reference configuration and $\boldsymbol{\sigma} = J^{-1}\mathbf{F}\mathbf{S}\mathbf{F}^{\mathrm{T}}$ is the Cauchy stress in the current configuration.

The symbols $\mathbf{B}_{\mathrm{R}}$ and $\mathbf{H}_{\mathrm{R}}$ in Fig. 8 denote the magnetic flux density and magnetic field strength in the reference configuration, respectively. The equivalent ones in the current configuration are $\mathbf{B}$ and $\mathbf{H}$. According to the nonlinear magneto-elastic interaction theory by Dorfmann and Ogden (2014), these four magnetic variables are connected by

$$\mathbf{B}_{\mathrm{R}} = J\mathbf{F}^{-1}\mathbf{B} \tag{3}$$

and

$$\mathbf{H}_{\mathrm{R}} = \mathbf{F}^{\mathrm{T}}\mathbf{H}. \tag{4}$$

The boundary conditions for $\mathbf{B}$ and $\mathbf{H}$ are

$$\mathbf{n}\times[\![\mathbf{H}]\!] = \mathbf{0} \tag{5}$$

and

$$\mathbf{n}\cdot[\![\mathbf{B}]\!] = 0, \tag{6}$$

where $[\![(\bullet)]\!] = (\bullet)_{\mathrm{outside}} - (\bullet)_{\mathrm{MRE}}$ and $\mathbf{n}$ is the normal direction at the interface between the isotropic s-MRE and the external environment. The symbols $\times$ and $\cdot$ are cross and dot product operators. In vacuum,

$$\mathbf{B} = \mu_0\mathbf{H}, \tag{7}$$

where $\mu_0 = 1.256\times10^{-6}$ T m A^{-1} is the permeability of vacuum.

3.2. Thermodynamic consistency

Following the standard convention of continuum mechanics, the Helmholtz free energy function is defined as the energy present per unit volume in the material. To depict the magnetic-dependent Mullins effect, viscoelasticity and the magnetization behaviour of the isotropic

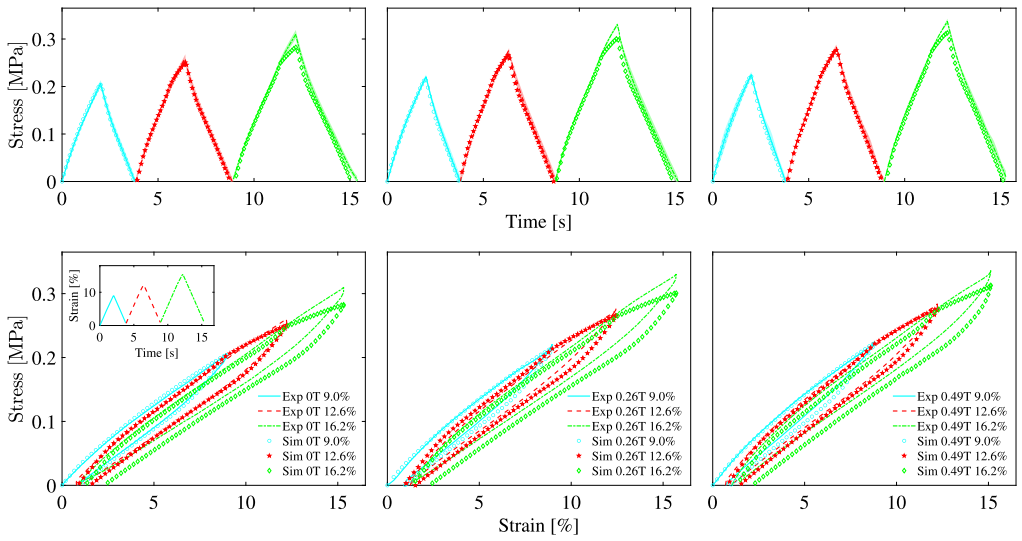

Fig. 7. Experimental (Exp) and simulation (Sim) results of dynamic loading tests (4.5×10^{-2} s^{-1}) under different magnetic fields (0, 0.26 and 0.49 T) with increasing strain amplitudes (9, 12.6 and 16.2%), where experimental scatter is shown in the light-coloured regions of the stress-time curves.

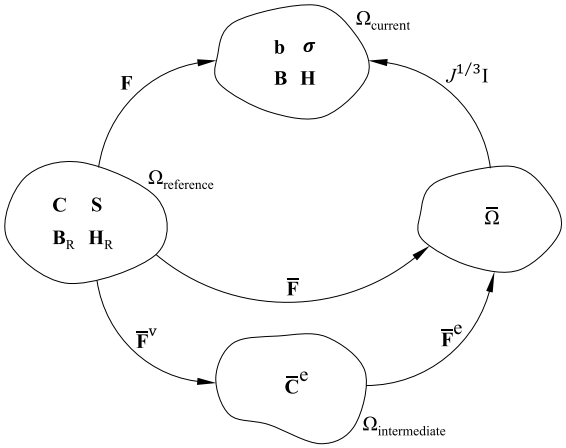

Fig. 8. Schematic configuration of the reference, intermediate and current configurations for isotropic s-MRE with the corresponding magnetic vectors and the stress and strain tensors.

s-MRE, the total Helmholtz free energy is decoupled into four parts as

$$\Psi = \Psi^{\text{Mullins}} + \Psi^{\text{magnetic}} + \Psi^{\text{mve}} + \Psi^{\text{vol}}, \tag{8}$$

where Ψ^{Mullins}, Ψ^{magnetic}, Ψ^{mve} and Ψ^{vol} denote the contribution to the total free energy from the magnetic-dependent Mullins effect, pure magnetic, magneto-viscoelastic and volume deformation, respectively. To depict the magneto-mechanical coupling behaviour of the isotropic s-MRE, the Helmholtz free energy is assumed to be a function of $\mathbf{C}$ and $\mathbf{H}_{\text{R}}$ (e.g., Bustamante (2010), Haldar et al. (2016) and Haldar (2021)). Subsequently, the corresponding Clausius-Plank inequality (Saxena et al., 2013; Haldar, 2021) is

$$-\dot{\Psi} - \mathbf{B}_{\text{R}} \cdot \dot{\mathbf{H}}_{\text{R}} + \frac{1}{2}\mathbf{S} : \dot{\mathbf{C}} \geq 0, \tag{9}$$

where : denotes the double contraction between two second-order tensors. Since the whole process is reversible for Ψ^{Mullins}, Ψ^{magnetic} and Ψ^{vol}, one obtains

$$-\dot{\Psi}^{\text{Mullins}} - \dot{\Psi}^{\text{magnetic}} - \dot{\Psi}^{\text{vol}} - \mathbf{B}_{\text{R}}^{\text{eq}} \cdot \dot{\mathbf{H}}_{\text{R}} + \frac{1}{2}\mathbf{S}^{\text{eq}} : \dot{\mathbf{C}} = 0, \tag{10}$$

where $\mathbf{B}_{\text{R}}^{\text{eq}}$ and $\mathbf{S}^{\text{eq}}$ are the magnetic flux density and the second Piola–Kirchhoff stress of the reversible process. By Eq. (10) with the chain rule method, $\mathbf{B}_{\text{R}}^{\text{eq}}$ and $\mathbf{S}^{\text{eq}}$ can be expressed as

$$\mathbf{B}_{\text{R}}^{\text{eq}} = \mathbf{B}_{\text{R}}^{\text{Mullins}} + \mathbf{B}_{\text{R}}^{\text{magnetic}} = -\frac{\partial \Psi^{\text{Mullins}}}{\partial \mathbf{H}_{\text{R}}} - \frac{\partial \Psi^{\text{magnetic}}}{\partial \mathbf{H}_{\text{R}}} \tag{11}$$

and

$$\mathbf{S}^{\text{eq}} = \mathbf{S}^{\text{Mullins}} + \mathbf{S}^{\text{magnetic}} + \mathbf{S}^{\text{vol}} = 2\frac{\partial \Psi^{\text{Mullins}}}{\partial \mathbf{C}} + 2\frac{\partial \Psi^{\text{magnetic}}}{\partial \mathbf{C}} + 2\frac{\partial \Psi^{\text{vol}}}{\partial \mathbf{C}}. \tag{12}$$

Conversely, due to the irreversibility of the viscoelastic process, the corresponding thermodynamic inequality for Ψ^{mve} is

$$-\dot{\Psi}^{\text{mve}} - \mathbf{B}_{\text{R}}^{\text{mve}} \cdot \dot{\mathbf{H}}_{\text{R}} + \frac{1}{2}\mathbf{S}^{\text{mve}} : \dot{\mathbf{C}} \geq 0. \tag{13}$$

Noting that Ψ^{mve} is determined by $\overline{\mathbf{C}}^{\text{e}}$ and $\mathbf{H}_{\text{R}}$. Hence, the time derivative of Ψ^{mve} can be expressed as

$$\dot{\Psi}^{\text{mve}} = \frac{\partial \Psi^{\text{mve}}}{\partial \overline{\mathbf{C}}^{\text{e}}} : \dot{\overline{\mathbf{C}}}^{\text{e}} + \frac{\partial \Psi^{\text{mve}}}{\partial \mathbf{H}_{\text{R}}} : \dot{\mathbf{H}}_{\text{R}}. \tag{14}$$

By Eq. (2), one has

$$\overline{\mathbf{C}}^{\text{e}} = \overline{\mathbf{F}}^{\text{v}^{-\text{T}}}\overline{\mathbf{C}}\overline{\mathbf{F}}^{\text{v}^{-1}}. \tag{15}$$

Following,

$$\dot{\overline{\mathbf{C}}}^{\text{e}} = -\overline{\mathbf{F}}^{\text{v}^{-\text{T}}}\dot{\overline{\mathbf{F}}^{\text{v}^{\text{T}}}}\overline{\mathbf{F}}^{\text{e}^{\text{T}}}\overline{\mathbf{F}}^{\text{e}} - \overline{\mathbf{F}}^{\text{e}^{\text{T}}}\overline{\mathbf{F}}^{\text{e}}\dot{\overline{\mathbf{F}}}^{\text{v}}\overline{\mathbf{F}}^{\text{v}^{-1}} + \overline{\mathbf{F}}^{\text{v}^{-\text{T}}}\dot{\overline{\mathbf{C}}}\overline{\mathbf{F}}^{\text{v}^{-1}}, \tag{16}$$

where $\dot{\overline{\mathbf{F}}^{\text{v}^{\text{T}}}}$ is the time derivative of $\overline{\mathbf{F}}^{\text{v}^{\text{T}}}$. Inserting Eqs. (14) and (16) into Eq. (13) and by

$$\frac{\partial \overline{\mathbf{C}}}{\partial \mathbf{C}} = J^{-2/3}\left(\mathbb{I} - \frac{1}{3}\mathbf{C} \otimes \mathbf{C}^{-1}\right) = J^{-2/3}\mathbb{P}^{\text{T}}, \tag{17}$$

where $\mathbb{P}$ is the transpose of the projection tensor to the reference configuration. $\mathbb{I}$ is the fourth-order unit tensor and the symbol $\otimes$ is the tensor product operator, one obtains

$$\mathbf{B}_{\text{R}}^{\text{mve}} = -\frac{\partial \Psi^{\text{mve}}}{\partial \mathbf{H}_{\text{R}}}, \tag{18}$$

$$\mathbf{S}^{\text{mve}} = 2J^{-2/3}\mathbb{P} : \overline{\mathbf{F}}^{\text{v}^{-1}}\frac{\partial \Psi^{\text{mve}}}{\partial \overline{\mathbf{C}}^{\text{e}}}\overline{\mathbf{F}}^{\text{v}^{-\text{T}}} \tag{19}$$

and a dissipation inequality

$$D^{\text{dissipation}} = \overline{\mathbf{F}}^{\text{e}}\frac{\partial \Psi^{\text{mve}}}{\partial \overline{\mathbf{C}}^{\text{e}}}\overline{\mathbf{F}}^{\text{e}^{\text{T}}} : \left(\overline{\mathbf{F}}^{\text{e}^{-\text{T}}}\overline{\mathbf{F}}^{\text{v}^{-\text{T}}}\dot{\overline{\mathbf{F}}^{\text{v}^{\text{T}}}}\overline{\mathbf{F}}^{\text{e}^{\text{T}}} + \overline{\mathbf{F}}^{\text{e}}\dot{\overline{\mathbf{F}}}^{\text{v}}\overline{\mathbf{F}}^{\text{v}^{-1}}\overline{\mathbf{F}}^{\text{e}^{-1}}\right) \geq 0. \tag{20}$$

The Kirchhoff viscoelastic stress $\boldsymbol{\tau}^{\mathrm{mve}}$ is defined as

$$\boldsymbol{\tau}^{\mathrm{mve}} = 2\overline{\mathbf{F}}^{\mathrm{e}} \frac{\partial \Psi^{\mathrm{mve}}}{\partial \overline{\mathbf{C}}^{\mathrm{e}}} \overline{\mathbf{F}}^{\mathrm{e^T}}. \tag{21}$$

Since the Kirchhoff viscoelastic stress $\boldsymbol{\tau}^{\mathrm{mve}}$ is symmetric tensor[1] and $\overline{\mathbf{F}}^{\mathrm{e}^{-\mathrm{T}}} \overline{\mathbf{F}}^{\mathrm{v}^{-\mathrm{T}}} \dot{\overline{\mathbf{F}}}^{\mathrm{v^T}} \overline{\mathbf{F}}^{\mathrm{e^T}} = \left(\overline{\mathbf{F}}^{\mathrm{e}} \dot{\overline{\mathbf{F}}}^{\mathrm{v}} \overline{\mathbf{F}}^{\mathrm{v}^{-1}} \overline{\mathbf{F}}^{\mathrm{e}^{-1}} \right)^{\mathrm{T}}$, the dissipation equation Eq. (20) can be expressed as

$$\begin{aligned} D^{\mathrm{dissipation}} &= \boldsymbol{\tau}^{\mathrm{mve}} : \frac{1}{2} \overline{\mathbf{F}}^{\mathrm{e}} \dot{\overline{\mathbf{F}}}^{\mathrm{v}} \overline{\mathbf{F}}^{\mathrm{v}^{-1}} \overline{\mathbf{F}}^{\mathrm{e^T}} \overline{\mathbf{F}}^{\mathrm{e}^{-\mathrm{T}}} \overline{\mathbf{F}}^{\mathrm{e}^{-1}} \\ &= \boldsymbol{\tau}^{\mathrm{mve}} : \frac{1}{2} \overline{\mathbf{F}}^{\mathrm{e}} \dot{\overline{\mathbf{F}}}^{\mathrm{v}} \overline{\mathbf{F}}^{\mathrm{v}^{-1}} \overline{\mathbf{F}}^{\mathrm{e^T}} \overline{\mathbf{b}}^{\mathrm{e}^{-1}} \\ &= \boldsymbol{\tau}^{\mathrm{mve}} \overline{\mathbf{b}}^{\mathrm{e}^{-1}} : \frac{1}{2} \overline{\mathbf{F}}^{\mathrm{e}} \dot{\overline{\mathbf{F}}}^{\mathrm{v}} \overline{\mathbf{F}}^{\mathrm{v}^{-1}} \overline{\mathbf{F}}^{\mathrm{e^T}}. \end{aligned} \tag{22}$$

$\overline{\mathbf{F}}^{\mathrm{e}} \dot{\overline{\mathbf{F}}}^{\mathrm{v}} \overline{\mathbf{F}}^{\mathrm{v}^{-1}} \overline{\mathbf{F}}^{\mathrm{e^T}}$ can be decoupled into symmetric and skew-symmetric parts as

$$\overline{\mathbf{F}}^{\mathrm{e}} \dot{\overline{\mathbf{F}}}^{\mathrm{v}} \overline{\mathbf{F}}^{\mathrm{v}^{-1}} \overline{\mathbf{F}}^{\mathrm{e^T}} = -\frac{1}{2} \overline{\mathbf{F}} \dot{\overline{\mathbf{C}}^{\mathrm{v}^{-1}}} \overline{\mathbf{F}}^{\mathrm{T}} + \mathrm{skw}\left(\overline{\mathbf{F}}^{\mathrm{e}} \dot{\overline{\mathbf{F}}}^{\mathrm{v}} \overline{\mathbf{F}}^{\mathrm{v}^{-1}} \overline{\mathbf{F}}^{\mathrm{e^T}} \right), \tag{23}$$

where skw(•) represents the skew-symmetric part of the tensor (•), and $\dot{\overline{\mathbf{C}}^{\mathrm{v}^{-1}}}$ is the time derivative of $\overline{\mathbf{C}}^{\mathrm{v}^{-1}}$. Due to the symmetry property of $\boldsymbol{\tau}^{\mathrm{mve}} \overline{\mathbf{b}}^{\mathrm{e}^{-1}}$, the skew-symmetric part of the tensor $\overline{\mathbf{F}}^{\mathrm{e}} \dot{\overline{\mathbf{F}}}^{\mathrm{v}} \overline{\mathbf{F}}^{\mathrm{v}^{-1}} \overline{\mathbf{F}}^{\mathrm{e^T}}$ does not play a role in Eq. (22). Therefore, by Eqs. (21) to (23), the dissipation inequality in Eq. (20) is simplified to

$$-\boldsymbol{\tau}^{\mathrm{mve}} \overline{\mathbf{b}}^{\mathrm{e}^{-1}} : \frac{1}{2} \overline{\mathbf{F}} \dot{\overline{\mathbf{C}}^{\mathrm{v}^{-1}}} \overline{\mathbf{F}}^{\mathrm{T}} \geq 0. \tag{24}$$

Since $\overline{\mathbf{F}} \dot{\overline{\mathbf{C}}^{\mathrm{v}^{-1}}} \overline{\mathbf{F}}^{\mathrm{T}} \overline{\mathbf{b}}^{\mathrm{e}^{-1}}$ is a deviatoric tensor, there is no contribution of the spherical part of $\boldsymbol{\tau}^{\mathrm{mve}}$ to the establishment of Eq. (24). Therefore, an alternative expression for Eq. (24) is

$$-\mathrm{dev}\left(\boldsymbol{\tau}^{\mathrm{mve}}\right) : \frac{1}{2} \overline{\mathbf{F}} \dot{\overline{\mathbf{C}}^{\mathrm{v}^{-1}}} \overline{\mathbf{F}}^{\mathrm{T}} \overline{\mathbf{b}}^{\mathrm{e}^{-1}} \geq 0. \tag{25}$$

To guarantee the thermodynamic inequality in Eq. (25), similar to the approach applied by Kaliske (2009), the evolution law is set to

$$-\frac{1}{2} \overline{\mathbf{F}} \dot{\overline{\mathbf{C}}^{\mathrm{v}^{-1}}} \overline{\mathbf{F}}^{\mathrm{T}} \overline{\mathbf{b}}^{\mathrm{e}^{-1}} = \dot{\gamma} \frac{\mathrm{dev}\left(\boldsymbol{\tau}^{\mathrm{mve}}\right)}{\left\| \mathrm{dev}\left(\boldsymbol{\tau}^{\mathrm{mve}}\right) \right\|}, \tag{26}$$

where symbols dev(•) and ‖•‖ denote the deviatoric and the Hilbert–Schmidt operators norm of the second-order tensor (•), respectively. $\dot{\gamma}$ denotes the effective creep rate. In order to satisfy the inequality in Eq. (20), $\dot{\gamma}$ is set to be a positive value.

4. Specific constitutive equations and model prediction

The specific constitutive equations corresponding to Ψ^{Mullins}, Ψ^{magnetic}, Ψ^{mve} and Ψ^{vol} are introduced in this section. After identifying the material parameters, the model simulation results are compared with the tested results. Furthermore, model verification and model prediction are conducted.

According to the representation theory of tensors and previous modelling studies of the isotropic s-MRE (e.g., Haldar (2021) and Lucarini et al. (2022b)), the tensor invariants

$$\overline{I}_1 = \mathrm{tr}\left(\overline{\mathbf{C}}\right), \quad \overline{I}_1^{\mathrm{e}} = \mathrm{tr}\left(\overline{\mathbf{C}}^{\mathrm{e}}\right), \quad I_3 = \det\left(\mathbf{C}\right), \tag{27}$$

$$I_4 = \mathbf{I} : \mathbf{H}_{\mathrm{R}} \otimes \mathbf{H}_{\mathrm{R}}, \quad I_5 = \mathbf{I} : \mathbf{H} \otimes \mathbf{H} = \mathbf{C}^{-1} : \mathbf{H}_{\mathrm{R}} \otimes \mathbf{H}_{\mathrm{R}} \tag{28}$$

are used to depict the magnetic-dependent mechanical behaviour of the isotropic s-MRE. The symbols det(•) and tr(•) represent the determinant and trace operator.

4.1. Constitutive equations of the magnetic-dependent Mullins effect and residual strain

According to the work by Lucarini et al. (2022b), without loss of generality, the pure magnetic free energy Ψ^{magnetic} can be expressed as

$$\Psi^{\mathrm{magnetic}}\left(I_5, J\right) = -m_0 m_1 \ln\left[\cosh\left(\frac{\sqrt{I_5}}{m_1}\right)\right] - \frac{\mu_0}{2} J I_5, \tag{29}$$

where the first term is used to describe the magnetization behaviour, and the second term represents the contribution of the Maxwell stress to the total stress. The two material parameters m_0 and m_1 are used to depict the magnetization behaviour of the material. Inserting Eq. (29) into Eqs. (11) and (12) with Eqs. (3), (4) and $\boldsymbol{\sigma} = J^{-1}\mathbf{F}\mathbf{S}\mathbf{F}^{\mathrm{T}}$, one obtains

$$\mathbf{B}^{\mathrm{magnetic}} = \left[J^{-1} m_0 \tanh\left(\frac{\sqrt{I_5}}{m_1}\right) \frac{1}{\sqrt{I_5}} + \mu_0 \right] \mathbf{H} \tag{30}$$

and

$$\boldsymbol{\sigma}^{\mathrm{magnetic}} = J^{-1} \left[m_0 \tanh\left(\frac{\sqrt{I_5}}{m_1}\right) \frac{1}{\sqrt{I_5}} + \mu_0 J \right] \mathbf{H} \otimes \mathbf{H} - \frac{\mu_0}{2} I_5 \mathbf{I}. \tag{31}$$

The volumetric free energy Ψ^{vol} is expressed as

$$\Psi^{\mathrm{vol}}\left(J\right) = 0.5K\left(J-1\right)^2, \tag{32}$$

where K is the bulk modulus of the material. The corresponding Cauchy stress $\boldsymbol{\sigma}^{\mathrm{vol}}$ is

$$\boldsymbol{\sigma}^{\mathrm{vol}} = K\left(J-1\right)\mathbf{I}. \tag{33}$$

Regarding the free energy to depict the Mullins effect and the residual strain, the previously proposed pseudo-elastic model by Dorfmann and Ogden (2004) is

$$\Psi^{\mathrm{Mullins}} = \eta_1 \Psi^{\mathrm{e}} + \left(1-\eta_2\right)\Psi^{\mathrm{residual}} + \varphi_1\left(\eta_1\right) + \varphi_2\left(\eta_2\right), \tag{34}$$

where Ψ^{e} is the elastic free energy function and Ψ^{residual} is introduced to describe the residual strain. η_1 and η_2 are internal variables used to describe the Mullins effect and residual strain, respectively.

In order to reveal the coupling relationship between the Mullins effect and the magnetic-dependence, the softening stress (the stress obtained from the virgin sample minus the stress after removal the Mullins effect) values under different magnetic fields are determined through the dynamic test data in Fig. 7. As shown in Fig. 9, a larger softening stress is encountered if a higher magnetic field is applied. To describe this trend, a magnetic-dependence mechanism should be included in the free energy function due to the Mullins effect. To depict the magnetic-dependence of the mechanical behaviour for the isotropic s-MRE, a modified pseudo-elastic model is proposed in the form of

$$\Psi^{\mathrm{Mullins}} = \eta_1 \Psi^{\mathrm{me}} + \left(1-\eta_2\right)\Psi^{\mathrm{residual}} + \varphi_1\left(\eta_1\right) + \varphi_2\left(\eta_2\right), \tag{35}$$

where Ψ^{me} is the free energy function to depict the magnetic-elastic behaviour. Specifically, as suggested by Saxena et al. (2013) and Haldar (2021), Ψ^{me} is obtained by multiplying Ψ^{e} with the magnetic-dependent term. Furthermore, a Yeoh model (Yeoh, 1993) is used to depict the hyperelastic behaviour of the isotropic s-MRE. Therefore, the specific form of Ψ^{me} is

$$\begin{aligned} \Psi^{\mathrm{me}} &= \left[1 + \mathrm{g_e} \tanh\left(\frac{\sqrt{I_4}}{M_{\mathrm{e}}}\right) \right] \Psi^{\mathrm{e}} \quad \text{with} \\ \Psi^{\mathrm{e}} &= \mu_{\mathrm{e}} \left[\left(\overline{I}_1 - 3\right) + d_2\left(\overline{I}_1 - 3\right)^2 + d_3\left(\overline{I}_1 - 3\right)^3 \right], \end{aligned} \tag{36}$$

[1] If Ψ is isotropic scalar function, the Kirchhoff viscoelastic stress $\boldsymbol{\tau} = 2\mathbf{F}\left(\partial\Psi/\partial\mathbf{C}\right)\mathbf{F}^{\mathrm{T}}$ can be written as $\boldsymbol{\tau} = \alpha_1\mathbf{I} + \alpha_2\mathbf{b} - \alpha_3\mathbf{b}^2$ (Dorfmann and Ogden, 2014), where α_i, $(i = 1, 2, 3)$ is a scalar function determined by I_1, I_2 and I_3.

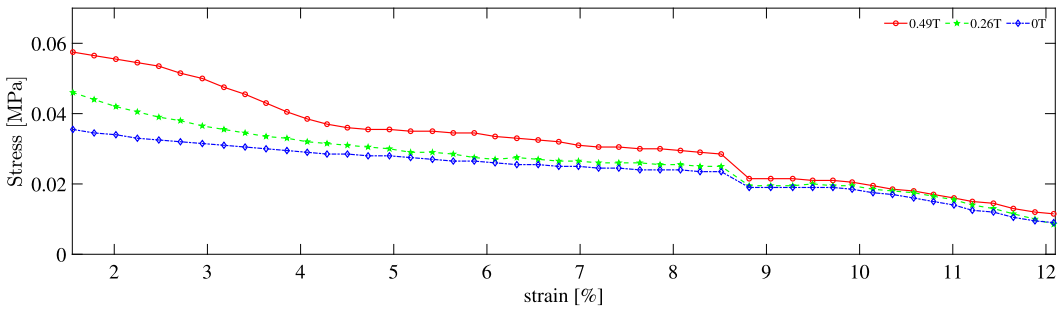

Fig. 9. Curves of the softening stress under different magnetic fields (0, 0.26 and 0.49 T).

where μ_e is the tensile modulus at zero magnetic field strength. Two material parameters d_2 and d_3 represent the contribution of the second- and third-order terms for $\left(\bar{I}_1 - 3\right)$ to the hyperelastic energy. g_e and M_e are material parameters to reflect the magnetic-dependence of the stress response.

According to Ogden and Roxburgh (1999), Dorfmann and Ogden (2004) and Fazekas and Goda (2021), the internal variable η_1 has two states (active or inactive), the state of η_1 is mediated by the relationship between the current strain and the historical maximum strain. Specifically, when the maximum historical strain gradually increases with loading, variable η_1 is inactive and the value is set to be 1. On the contrary, when the maximum historical strain does not change with loading, the value of η_1 is activated and updates as

$$\eta_1 = 1 - \frac{1}{q}\mathrm{erf}\left[\frac{\Psi^{e}_{max} - \Psi^{e}\left(\bar{I}_1\right)}{w}\right], \tag{37}$$

where $0 < \eta_1 \leq 1$ and $\mathrm{erf}[\bullet]$ is the Gauss error function. q and w are positive parameters. Ψ^{e}_{max} is the maximum value of Ψ^{e} at the current loading history. Following the path by (Dorfmann and Ogden, 2004),

$$\frac{\partial \Psi^{\mathrm{Mullins}}}{\partial \eta_1} = 0. \tag{38}$$

Inserting Eqs. (35) and (36) into Eq. (38) and by Eq. (37), one obtains

$$\begin{aligned}\frac{\partial \varphi_1(\eta_1)}{\partial \eta_1} &= -\Psi^{\mathrm{me}} \\ &= -\left[1 + g_e \tanh\left(\frac{\sqrt{I_4}}{M_e}\right)\right]\left\{\Psi^{e}_{max} - w \cdot \mathrm{erf}^{-1}\left[q\left(1-\eta_1\right)\right]\right\},\end{aligned} \tag{39}$$

The specific form of $\varphi_1(\eta_1)$ can be obtained by solving the nonlinear equation in Eq. (39).[2]

To describe the residual strain, a negative value of the stress at zero deformation is required (Dorfmann and Ogden, 2004). the corresponding free energy function Ψ^{residual} is

$$\begin{aligned}\Psi^{\mathrm{residual}} &= \mu_e\left[\bar{I}_1^{\mathrm{modi}} + d_2\left(\bar{I}_1^{\mathrm{modi}}\right)^2 + d_3\left(\bar{I}_1^{\mathrm{modi}}\right)^3\right], \\ \bar{I}_1^{\mathrm{modi}} &= \nu_1\left(\tilde{\lambda}_1^2 - 1\right) + \nu_2\left(\tilde{\lambda}_2^2 - 1\right) + \nu_3\left(\tilde{\lambda}_3^2 - 1\right),\end{aligned} \tag{40}$$

where $\bar{I}_1^{\mathrm{modi}}$ is a modified form of $\left(\bar{I}_1 - 3\right)$ and $\tilde{\lambda}_i^2$, $(i = 1, 2, 3)$ is the eigenvalue of $\bar{\mathbf{C}}$. The material parameter ν_i is expressed as

$$\nu_i = \kappa_1 + \kappa_2 \tanh\left(\frac{\lambda_{i,\max} - 1}{\kappa_3}\right), \tag{41}$$

where κ_i is a non-dimensional model parameter and $\lambda_{i,\max}$ is the maximum value of the principal strain λ_i acting in the ith direction.

[2] Eqs. (39) and (44) are needed only for demonstration purposes. Since $\varphi_1(\eta_1)$ and $\varphi_2(\eta_2)$ do not participate in the subsequent numerical realization calculations, their specific forms are not shown.

Subsequently, similar to η_1, the internal variable η_2 is a fixed value of 1 in the inactive state and updates in the active state according to

$$\eta_2 = \frac{\tanh\left[\left(\frac{\Psi^{e}\left(\bar{I}_1\right)}{\Psi^{e}_{max}}\right)^{\frac{\alpha \Psi^{e}_{max}}{\mu_e}}\right]}{\tanh(1)}, \tag{42}$$

where $0 < \eta_2 \leq 1$ and α is a non-dimensional parameter. In addition, the condition that η_2 satisfies is

$$\frac{\partial \Psi^{\mathrm{Mullins}}}{\partial \eta_2} = 0. \tag{43}$$

Inserting Eq. (35) into Eq. (43), results

$$\frac{\partial \varphi_2(\eta_2)}{\partial \eta_2} = \Psi^{\mathrm{residual}}. \tag{44}$$

Similar to Eq. (39), analytically, the specific form of $\varphi_2(\eta_2)$ can be obtained by solving Eq. (44). Inserting Eqs. (35), (36) and (40) into Eqs. (11) and (12) with Eqs. (3), (4) and $\boldsymbol{\sigma} = J^{-1}\mathbf{F}\mathbf{S}\mathbf{F}^{\mathrm{T}}$, the corresponding magnetic flux density $\mathbf{B}^{\mathrm{Mullins}}$ and Cauchy stress $\boldsymbol{\sigma}^{\mathrm{Mullins}}$ are

$$\begin{aligned}\mathbf{B}^{\mathrm{Mullins}} = &\frac{J^{-1}\eta_1\mu_e g_e \mathbf{b}\mathbf{H}}{\sqrt{I_4}M_e}\left[\tanh^2\left(\frac{\sqrt{I_4}}{M_e}\right) - 1\right] \\ &\times\left[\left(\bar{I}_1 - 3\right) + d_2\left(\bar{I}_1 - 3\right)^2 + d_3\left(\bar{I}_1 - 3\right)^3\right]\end{aligned} \tag{45}$$

and

$$\begin{aligned}\boldsymbol{\sigma}^{\mathrm{Mullins}} = &2J^{-1}\eta_1\left[1 + g_e\tanh\left(\frac{\sqrt{I_4}}{M_e}\right)\right]\frac{\partial \Psi^{e}}{\partial \bar{I}_1}\mathrm{dev}(\bar{\mathbf{b}}) \\ &+ 2J^{-1}\left(1 - \eta_2\right)\frac{\partial \Psi^{\mathrm{residual}}}{\partial \bar{I}_1^{\mathrm{modi}}}\mathrm{dev}\left(\tilde{\mathbf{b}}\right)\end{aligned} \tag{46}$$

with

$$\frac{\partial \Psi^{e}}{\partial \bar{I}_1} = \mu_e\left[1 + 2d_2\left(\bar{I}_1 - 3\right) + 3d_3\left(\bar{I}_1 - 3\right)^2\right], \tag{47}$$

$$\frac{\partial \Psi^{\mathrm{residual}}}{\partial \bar{I}_1^{\mathrm{modi}}} = \mu_e\left[1 + 2d_2\bar{I}_1^{\mathrm{modi}} + 3d_3\left(\bar{I}_1^{\mathrm{modi}}\right)^2\right] \tag{48}$$

and

$$\tilde{\mathbf{b}} = \begin{bmatrix}\nu_1\tilde{\lambda}_1^2 & 0 & 0 \\ 0 & \nu_2\tilde{\lambda}_2^2 & 0 \\ 0 & 0 & \nu_3\tilde{\lambda}_3^2\end{bmatrix}. \tag{49}$$

4.2. Constitutive equations to depict the magnetic-dependent nonlinear viscoelastic behaviour

To reflect the magnetic-dependence of the viscoelastic free energy, the viscoelastic stress (the total stress response of the dynamic test in Fig. 7 minus the hyperelastic stress response of the quasi-static test in Fig. 5) values under different magnetic fields are determined through experimental test data. As shown in Fig. 10, a larger viscoelastic

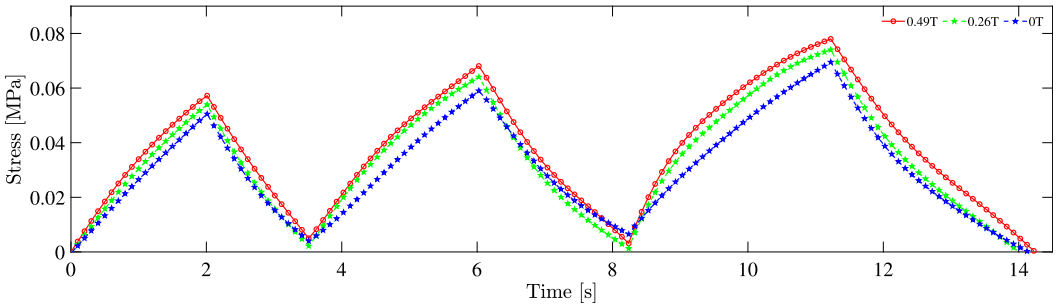

Fig. 10. Curves of the viscoelastic stress under different magnetic fields (0, 0.26 and 0.49 T).

response is obtained if a higher magnetic field is applied. Therefore, a magnetic-dependence is directly introduced into the viscoelastic free energy term to depict this observed experimental phenomenon. Similar to the form of the magnetic-dependent hyperelastic free energy in Eq. (36), the magnetic-dependent viscoelastic free energy Ψ^{mve} is

$$\begin{aligned}\Psi^{\mathrm{mve}} &= \left[1+\mathrm{g}_{\mathrm{ve}}\tanh\left(\frac{\sqrt{I_4}}{M_{\mathrm{ve}}}\right)\right]\Psi^{\mathrm{ve}},\\ \Psi^{\mathrm{ve}} &= \mu_{\mathrm{ve}}\left[\left(\overline{I}_1^{\mathrm{e}}-3\right)+d_2\left(\overline{I}_1^{\mathrm{e}}-3\right)^2+d_3\left(\overline{I}_1^{\mathrm{e}}-3\right)^3\right].\end{aligned} \tag{50}$$

Inserting Eq. (50) into Eqs. (18) and (19) with Eqs. (3), (4) and $\boldsymbol{\sigma} = J^{-1}\mathbf{F}\mathbf{S}\mathbf{F}^{\mathrm{T}}$, the corresponding magnetic flux density $\mathbf{B}^{\mathrm{mve}}$ and Cauchy stress $\boldsymbol{\sigma}^{\mathrm{mve}}$ are

$$\begin{aligned}\mathbf{B}^{\mathrm{mve}} = {}& \frac{J^{-1}\mu_{\mathrm{ve}}\mathrm{g}_{\mathrm{ve}}\mathbf{b}\mathbf{H}}{\sqrt{I_4}M_{\mathrm{ve}}}\left[\tanh^2\left(\frac{\sqrt{I_4}}{M_{\mathrm{ve}}}\right)-1\right]\\ &\times\left[\left(\bar{I}_1^{\mathrm{e}}-3\right)+d_2\left(\bar{I}_1^{\mathrm{e}}-3\right)^2+d_3\left(\bar{I}_1^{\mathrm{e}}-3\right)^3\right]\end{aligned} \tag{51}$$

and

$$\begin{aligned}\boldsymbol{\sigma}^{\mathrm{mve}} = {}& 2J^{-1}\mu_{\mathrm{ve}}\left[1+\mathrm{g}_{\mathrm{ve}}\tanh\left(\frac{\sqrt{I_4}}{M_{\mathrm{ve}}}\right)\right]\\ &\left[1+2d_2\left(\overline{I}_1^{\mathrm{e}}-3\right)+3d_3\left(\overline{I}_1^{\mathrm{e}}-3\right)^2\right]\mathrm{dev}\left(\overline{\mathbf{b}}^{\mathrm{e}}\right).\end{aligned} \tag{52}$$

Inserting Eq. (50) into Eq. (21), an alternative expression for Eq. (26) is

$$-\frac{1}{2}\dot{\overline{\mathbf{F}\mathbf{C}^{\mathrm{v}^{-1}}\mathbf{F}^{\mathrm{T}}}}\overline{\mathbf{b}}^{\mathrm{e}^{-1}} = \dot{\gamma}\frac{\mathrm{dev}\left(\overline{\mathbf{b}}^{\mathrm{e}}\right)}{\left\|\mathrm{dev}\left(\overline{\mathbf{b}}^{\mathrm{e}}\right)\right\|}. \tag{53}$$

In order to depict the nonlinear viscoelastic behaviour of the isotropic s-MRE, a strain process-dependence (e.g., Bergström and Boyce (1998), Kaliske (2009) and Wang et al. (2023)) is introduced for the effective creep rate $\dot{\gamma}$. The form of $\dot{\gamma}$ is assumed to be

$$\dot{\gamma} = \dot{\gamma}_0\left[\sqrt{\frac{\overline{I}_1^{\mathrm{v}}}{3}}-1\right]^c\left(\frac{\left\|\mathrm{dev}\left(\overline{\mathbf{b}}^{\mathrm{e}}\right)\right\|}{\sqrt{2}}\right)^m, \tag{54}$$

where $\dot{\gamma}_0 > 0$ is the reference effective creep rate and $\overline{I}_1 = \mathrm{tr}\left(\overline{\mathbf{C}}^{\mathrm{v}}\right)$. Power term $c \in [-1, 0]$ determines the kinetics of relaxation, and $m \in [1, +\infty]$ determines the strain-activated inelastic process. In Eq. (54), the effect creep rate $\dot{\gamma}$ decreases with increasing viscous strain and increases with increasing elastic strain. The viscoelastic constitutive equation in Eq. (53) is highly nonlinear. In order to solve it, the operator splitting method (e.g., Simo and Hughes (2006), Nguyen et al. (2007) and Reese and Govindjee (1998)) is applied. The detailed numerical integration algorithm corresponding to the operator splitting method is presented in Appendix.

In summary, the constitutive equations to depict the nonlinear magneto-mechanical behaviour of the isotropic s-MRE are

$$\begin{cases}\boldsymbol{\sigma} = \boldsymbol{\sigma}^{\mathrm{Mullins}} + \boldsymbol{\sigma}^{\mathrm{mve}} + \boldsymbol{\sigma}^{\mathrm{vol}} + \boldsymbol{\sigma}^{\mathrm{magnetic}}\\ \boldsymbol{\sigma}^{\mathrm{vol}} = K(J-1)\mathbf{I}\\ \boldsymbol{\sigma}^{\mathrm{magnetic}} = J^{-1}\left[m_0\tanh\left(\frac{\sqrt{I_5}}{m_1}\right)\frac{1}{\sqrt{I_5}}+\mu_0 J\right]\mathbf{H}\otimes\mathbf{H}-0.5\mu_0 I_5\mathbf{I}\\ \boldsymbol{\sigma}^{\mathrm{Mullins}} = 2J^{-1}\eta_1\left[1+\mathrm{g}_{\mathrm{e}}\tanh\left(\frac{\sqrt{I_4}}{M_{\mathrm{e}}}\right)\right]\frac{\partial\Psi^{\mathrm{e}}}{\partial\bar{I}_1}\mathrm{dev}\left(\bar{\mathbf{b}}\right)\\ +2J^{-1}\left(1-\eta_2\right)\frac{\partial\Psi^{\mathrm{residual}}}{\partial\bar{I}_1^{\mathrm{modi}}}\mathrm{dev}\left(\bar{\mathbf{b}}\right)\\ \frac{\partial\Psi^{\mathrm{e}}}{\partial\bar{I}_1} = \mu_{\mathrm{e}}\left[1+2d_2\left(\overline{I}_1-3\right)+3d_3\left(\overline{I}_1-3\right)^2\right]\\ \frac{\partial\Psi^{\mathrm{residual}}}{\partial\bar{I}_1^{\mathrm{modi}}} = \mu_{\mathrm{e}}\left[1+2d_2\overline{I}_1^{\mathrm{modi}}+3d_3\left(\overline{I}_1^{\mathrm{modi}}\right)^2\right]\\ \eta_1 = 1-\frac{1}{q}\mathrm{erf}\left[\frac{\Psi^{\mathrm{e}}_{\max}-\Psi^{\mathrm{e}}\left(\bar{I}_1\right)}{w}\right]\\ \eta_2 = \tanh\left\{\left[\Psi^{\mathrm{e}}\left(\bar{I}_1\right)/\Psi^{\mathrm{e}}_{\max}\right]^{\frac{\alpha\Psi^{\mathrm{e}}_{\max}}{\mu_{\mathrm{e}}}}\right\}/\tanh(1)\\ \nu_i = \kappa_1+\kappa_2\tanh\left(\frac{\lambda_{i,\max}-1}{\kappa_3}\right),\ (i=1,2,3)\\ \boldsymbol{\sigma}^{\mathrm{mve}} = 2J^{-1}\mu_{\mathrm{ve}}\left[1+\mathrm{g}_{\mathrm{ve}}\tanh\left(\frac{\sqrt{I_4}}{M_{\mathrm{ve}}}\right)\right]\\ \left[1+2d_2\left(\overline{I}_1^{\mathrm{e}}-3\right)+3d_3\left(\overline{I}_1^{\mathrm{e}}-3\right)^2\right]\mathrm{dev}\left(\overline{\mathbf{b}}^{\mathrm{e}}\right)\\ -\frac{1}{2}\dot{\overline{\mathbf{F}\mathbf{C}^{\mathrm{v}^{-1}}\mathbf{F}^{\mathrm{T}}}}\overline{\mathbf{b}}^{\mathrm{e}^{-1}} = \dot{\gamma}\frac{\mathrm{dev}\left(\overline{\mathbf{b}}^{\mathrm{e}}\right)}{\left\|\mathrm{dev}\left(\overline{\mathbf{b}}^{\mathrm{e}}\right)\right\|},\ \dot{\gamma} = \dot{\gamma}_0\left[\sqrt{\frac{\overline{I}_1^{\mathrm{v}}}{3}}-1\right]^c\left(\frac{\left\|\mathrm{dev}\left(\overline{\mathbf{b}}^{\mathrm{e}}\right)\right\|}{\sqrt{2}}\right)^m\end{cases}. \tag{55}$$

4.3. Boundary value problem solutions and parameter identification

For obtaining the solution to the boundary value problem, it is assumed $J = 1$. As shown in Fig. 3, the uniaxial tension is along the y-direction. Therefore, the corresponding deformation gradient is

$$\mathbf{F} = \begin{bmatrix}\lambda^{-0.5} & 0 & 0\\ 0 & \lambda & 0\\ 0 & 0 & \lambda^{-0.5}\end{bmatrix}, \tag{56}$$

where $\lambda > 1$ is the stretch along the y-direction. In order to conduct the parameter identification, besides $\mathbf{F}$, the magnetic field strength within MRE should be determined as well. A detailed introduction of the

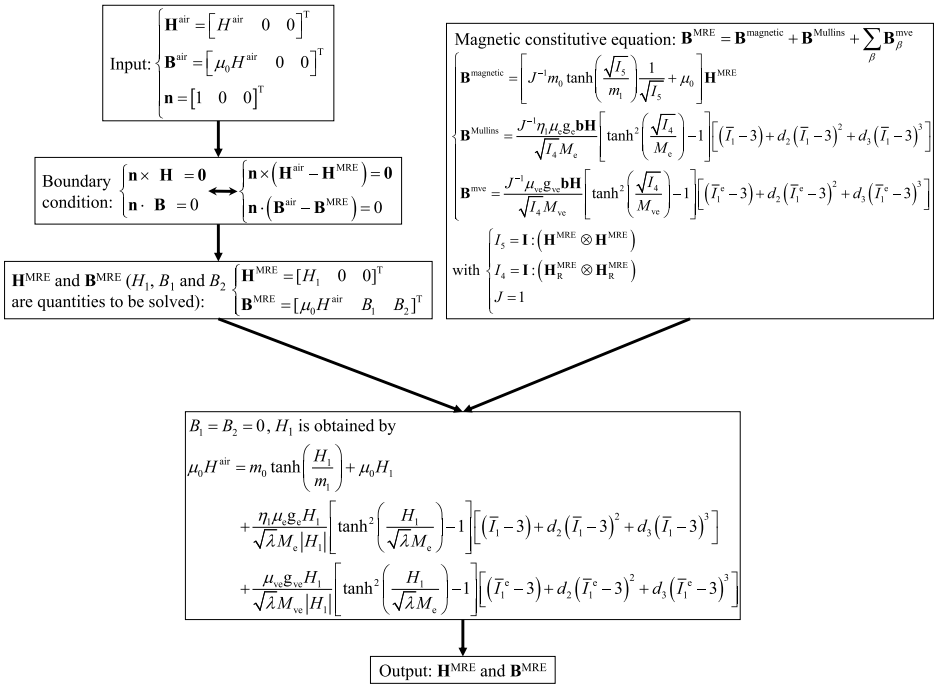

Fig. 11. Flowchart for solving the magnetic boundary value problem.

method to determine the magnetic field strength within MRE through the tested magnetic field strength in the air can be found in Dorfmann and Ogden (2014) and Bustamante (2010). To ease the understanding of readers, a flow chart corresponding to this method is shown in Fig. 11 and the corresponding explanation is as follows.

As shown in Fig. 3, the applied magnetic field in the air is along the x-direction and can be expressed as

$$\mathbf{H}^{\text{air}} = \begin{bmatrix} H^{\text{air}} & 0 & 0 \end{bmatrix}^{\text{T}}, \tag{57}$$

where H^{air} is the magnetic field strength in the external environment. By Eq. (7), the magnetic flux density $\mathbf{B}^{\text{air}}$ is

$$\mathbf{B}^{\text{air}} = \mu_0 \mathbf{H}^{\text{air}} = \begin{bmatrix} \mu_0 H^{\text{air}} & 0 & 0 \end{bmatrix}^{\text{T}}. \tag{58}$$

The direction $\mathbf{n}$ of the magnetic flux density at the interface between the isotropic s-MRE and the air is

$$\mathbf{n} = [1 \quad 0 \quad 0]^{\text{T}}. \tag{59}$$

By the boundary conditions in Eqs. (5) and (6), the magnetic field strength $\mathbf{H}^{\text{MRE}}$ and magnetic flux density $\mathbf{B}^{\text{MRE}}$ within the isotropic s-MRE are

$$\mathbf{H}^{\text{MRE}} = [H_1 \quad 0 \quad 0]^{\text{T}} \tag{60}$$

and

$$\mathbf{B}^{\text{MRE}} = [\mu_0 H^{\text{air}} \quad B_1 \quad B_2]^{\text{T}}. \tag{61}$$

where H_1, B_1 and B_2 are the variables to solve for. According to Eqs. (4), (56) and (60), I_4 and I_5 can be simplified as

$$I_4 = \lambda^{-1} H_1^2 \tag{62}$$

and

$$I_5 = H_1^2. \tag{63}$$

Subsequently, the magnetic flux density of the isotropic s-MRE determined by the constitutive equation is

$$\mathbf{B}^{\text{MRE}} = \mathbf{B}^{\text{magnetic}} + \mathbf{B}^{\text{Mullins}} + \sum_{\beta} \mathbf{B}_{\beta}^{\text{mve}}, \tag{64}$$

where β is the number of viscoelastic elements set. The specific form for $\mathbf{B}^{\text{MRE}}$ is shown in Fig. 11. Substituting Eqs. (60) to (63) and the incompressibility condition $J = 1$ into Eq. (64), results

$$B_1 = B_2 = 0 \tag{65}$$

and

$$\begin{aligned} \mu_0 H^{\text{air}} = {} & m_0 \tanh\left(\frac{H_1}{m_1}\right) + \mu_0 H_1 \\ & + \frac{\eta_1 \mu_{\text{e}} g_{\text{e}} H_1}{\sqrt{\lambda} M_{\text{e}} |H_1|} \left[\tanh^2\left(\frac{H_1}{\sqrt{\lambda} M_{\text{e}}}\right) - 1\right] \\ & \times \left[(\bar{I}_1 - 3) + d_2 (\bar{I}_1 - 3)^2 + d_3 (\bar{I}_1 - 3)^3\right] \\ & + \sum_{\beta} \frac{\mu_{\text{ve}}^{\beta} g_{\text{ve}}^{\beta} H_1}{\sqrt{\lambda} M_{\text{ve}}^{\beta} |H_1|} \left[\tanh^2\left(\frac{H_1}{\sqrt{\lambda} M_{\text{ve}}^{\beta}}\right) - 1\right] \\ & \times \left[\left(\bar{I}_{1\beta}^{\text{e}} - 3\right) + d_{2\beta}\left(\bar{I}_{1\beta}^{\text{e}} - 3\right)^2 + d_{3\beta}\left(\bar{I}_{1\beta}^{\text{e}} - 3\right)^3\right]. \end{aligned} \tag{66}$$

With known H^{air}, H_1 can be obtained by solving Eq. (66)[3] through Newton–Raphson method.

After obtaining the magnetic field strength of the material, the Cauchy stress is calculated, and its expression is

$$\boldsymbol{\sigma} = \boldsymbol{\sigma}^{\text{Mullins}} + \boldsymbol{\sigma}^{\text{mve}} - p\mathbf{I}, \tag{67}$$

[3] In the subsequent parameter identification, it is found that the contribution of the applied magnetic field is mainly reflected in the magnetic flux density $\mathbf{B}^{\text{magnetic}}$ of the purely magnetic part. After calculation, it is found that the contribution to the magnetic flux density by $\mathbf{B}^{\text{magnetic}}$ is at least two orders higher than $\mathbf{B}^{\text{Mullins}}$ and $\mathbf{B}^{\text{mve}}$ for the given strain range (less than 18%). Therefore, H_1 can be solved approximately by $\mu_0 H^{\text{air}} \approx m_0 \tanh(H_1/m_1) + \mu_0 H_1$.

where p can be identified as a hydrostatic pressure. Due to the traction-free boundary condition $\sigma_{11} = \sigma_{33} = 0$, one obtains

$$p = \sigma_{11}^{\text{Mullins}} + \sigma_{11}^{\text{mve}} = \sigma_{33}^{\text{Mullins}} + \sigma_{33}^{\text{mve}}. \tag{68}$$

Inserting Eq. (68) into Eq. (67), results

$$\sigma_{22} = \sigma_{22}^{\text{mve}} - \sigma_{11}^{\text{mve}} + \sigma_{22}^{\text{Mullins}} - \sigma_{11}^{\text{Mullins}}. \tag{69}$$

By inserting Eqs. (56) and (60) into Eq. (55) and $J = 1$, the specific form of each item in σ_{22} is

$$\begin{aligned}\sigma_{22}^{\text{mve}} - \sigma_{11}^{\text{mve}} = 2\mu_{\text{ve}} &\left[1 + g_{\text{ve}} \tanh\left(\frac{H_1}{M_{\text{ve}}}\right)\right] \\ &\times \left[1 + 2d_2\left(\lambda^{e^2} + 2\frac{1}{\lambda^{\text{e}}} - 3\right)\right. \\ &\left. + 3d_3\left(\lambda^{e^2} + 2\frac{1}{\lambda^{\text{e}}} - 3\right)^2\right]\left(\lambda^{e^2} - \frac{1}{\lambda^{\text{e}}}\right)\end{aligned} \tag{70}$$

and

$$\begin{aligned}\sigma_{22}^{\text{Mullins}} - \sigma_{11}^{\text{Mullins}} = 2\eta_1 &\left[1 + g_{\text{e}} \tanh\left(\frac{H_1}{M_{\text{e}}}\right)\right] \frac{\partial \Psi^{\text{e}}}{\partial \bar{I}_1}\left(\lambda^2 - \frac{1}{\lambda}\right) \\ &+ 2(1-\eta_2)\frac{\partial \Psi^{\text{residual}}}{\partial \bar{I}_1^{\text{modi}}}\left(\nu_2\lambda^2 - \nu_1\frac{1}{\lambda}\right)\end{aligned} \tag{71}$$

with

$$\begin{aligned}\frac{\partial \Psi^{\text{e}}}{\partial \bar{I}_1} &= \mu_{\text{e}}\left[1 + 2d_2\left(\lambda^2 + 2\frac{1}{\lambda} - 3\right) + 3d_3\left(\lambda^2 + 2\frac{1}{\lambda} - 3\right)^2\right], \\ \frac{\partial \Psi^{\text{residual}}}{\partial \bar{I}_1^{\text{modi}}} &= \mu_{\text{e}}\left[1 + 2d_2\left(\nu_1\lambda^2 - \nu_1 + 2\nu_2\frac{1}{\lambda} - 2\nu_2\right)\right. \\ &\quad \left. + 3d_3\left(\nu_1\lambda^2 - \nu_1 + 2\nu_2\frac{1}{\lambda} - 2\nu_2\right)^2\right],\end{aligned} \tag{72}$$

where the parameter ν_1 satisfies $\nu_1 = \kappa_1$ under the uniaxial tensile test condition (Dorfmann and Ogden, 2004).

The nonlinear least square fitting method by the function `lsqnonlin` in MATLAB® (MATLAB Release 2020b, The MathWorks, Inc., Natick, Massachusetts, United States) is applied to obtain the material parameters which describe the magneto-mechanical coupling behaviour of the isotropic s-MRE. The detailed parameter identification is as follows. Firstly, the values of parameters m_0 and m_1 are obtained from the magnetic test result as shown in Fig. 2 with Eq. (30). After identifying m_0 and m_1, the magnetic field strength H_1 within the isotropic s-MRE are obtained by solving Eq. (66). Regarding the parameters describing the magnetic-dependent Mullins effect and the residual strain of the isotropic s-MRE, the magnetic independent material parameters μ_{e}, d_2, d_3, q, w, α and $\kappa_i\,(i = 1, 2, 3)$ are identified by the results in Fig. 5 under 0 T with Eqs. (71) and (72). Afterwards, the magnetic-dependent parameters g_{e} and M_{e} are identified by the results in Fig. 5 under 0.26 and 0.49 T magnetic fields. In this work, the maximum magnetic field during the quasi-static test is 0.49 T, which is smaller than the saturation magnetization intensity for the isotropic s-MRE. Hence, the parameter M_{e} is set to $\mu_0 M_{\text{e}} = 1$ T. The comparison between the simulation and experimental results is shown in Fig. 5. Clearly, the proposed magnetic-dependent pseudo-elastic model can accurately depict the magnetic-dependent Mullins effect and residual strain of the isotropic s-MRE with accuracy.

Regarding the identification of the viscoelastic parameters, two sets of process-dependent viscoelastic elements with constitutive equations in Eq. (70) are utilized to depict the magnetic-dependent viscoelastic behaviour of the isotropic s-MRE. Firstly, the magnetic-independent material parameters μ_{ve}, $\dot{\gamma}_0$, c and m are identified by the stress relaxation result under 0 T as shown in Fig. 6. After obtaining the values of the magnetic independent material parameters, the magnetic-dependent parameter g_{ve} and M_{ve} are identified by the results under 0.26 and 0.49 T in Fig. 6. Similar to the above mentioned setup, M_{ve} is set to $\mu_0 M_{\text{ve}} = 1$ T. The comparison between the simulation and experimental results is shown in Fig. 6. Apparently, the magnetic-dependent viscoelastic behaviour of the isotropic s-MRE is well depicted by the developed model.

As a comparison study, four sets of classical Maxwell viscoelastic elements[4] are utilized to depict the magnetic-dependent viscoelastic behaviour of the isotropic s-MRE and the comparison between simulation and experimental results is shown in Fig. 12. The R-squared and mean absolute percentage error (MAPE) of the two models are calculated with the experimental results and simulation results of stress relaxation. The R-squared and MAPE values of the process-dependent viscoelastic model are 0.997 and 1.10%, respectively, and the corresponding quantities of the classical Maxwell viscoelastic model are 0.969 and 3.17%, respectively. Comparing the values of R-squared and MAPE, it can be found that even though two more material parameters in the classical Maxwell viscoelastic model are applied, the fitting result is not as good as the process-dependent viscoelastic model. The specific values of the material parameters obtained by identification and the determination coefficient with R-squared and MAPE between simulation and test result are shown in Table 1.

4.4. Model verification and prediction

In practice, the Mullins effect, residual strain and the nonlinear viscoelastic behaviour of the material occur in a simultaneous manner. To validate the prediction ability of the proposed model, a triangular strain loading with increasing strain amplitudes (9, 12.6 and 16.2%) at a relatively fast loading rate (4.5×10^{-2} s^{-1}) is conducted for the test sample. The identified material parameters in Table 1 are used to predict the stress response. The comparison between simulation and experimental results is shown in Fig. 7, and the corresponding R-squared value is calculated, which is 0.985. By analysing the data results and R-squared, the simulation results fit well with the experimental results.

Moreover, in order to verify the predictive ability of the proposed model for viscoelasticity, sinusoidal tests with different loading frequencies (1, 0.1 and 0.01 Hz), loading amplitudes (9.0, 12.6 and 16.2%) and magnetic field (0, 0.26 and 0.49 T) are carried out. To obtain stable stress–strain results, the test cycles are set to 5 cycles for 0.01 Hz, 30 cycles for 0.1 Hz and 100 cycles for 1 Hz according to the loading frequency. Subsequently, the corresponding stress responses are calculated with the proposed model and the parameter values in Table 1. The experimental results and predicted results are shown in Fig. 13, and the corresponding R-squared value is calculated, which is 0.989. The value of R-squared illustrates that the proposed model has a good fitting effect.

Furthermore, a predicted case is used to illustrate the contribution of loading history and magnetic field to the stress response. For this case, two cycles of triangular are considered. Specifically, three levels of strain amplitude which are 4, 8 and 16%, are applied for the first cycle of the strain loading and the strain amplitude of the second cycle is fixed to 8%. The stress response of the second cycle is used to illustrate the effect of loading history on the stress-softening behaviour of the material. During the simulation, the effects of different magnetic fields (0 and 1 T) are considered. The results for this simulation case are shown in Fig. 14. It is found that a larger value of maximum history strain leads to a more pronounced stress softening and residual strain.

5. Conclusion and outlook

In this work, the magnetic-dependent inelastic mechanical behaviours of the isotropic s-MRE are tested through a DMA with magnetic field excitation and DIC strain measurement components.

[4] By setting $c = 0$ and $m = 1$ in Eq. (54), the process-dependent viscoelastic model is degraded into the classical Maxwell viscoelastic model as proposed by Reese and Govindjee (1998).

Table 1
Specific values of material parameters involved in inelastic behaviours of the isotropic s-MRE with R-squared and mean absolute percentage error (MAPE).

Model utilized	Identified parameters	R-squared/MAPE
Magnetization model	$m_0 = 4.494 \times 10^{-1}$ T, $m_1 = 2.615 \times 10^{2}$ kA/m	0.999/7.17%
Magnetic-dependent pseudo-elastic model	$\mu_e = 3.287 \times 10^{5}$ Pa, $d_2 = -2.590$, $d_3 = 6.442$ $g_e = 5.282 \times 10^{-1}$, $q = 1.731 \times 10$, $w = 3.480 \times 10^{3}$ Pa $\alpha = 3.605 \times 10^{-1}$, $\kappa_1 = 2.311$, $\kappa_2 = 3.138$ $\kappa_3 = 1.200 \times 10^{-3}$	0.986/14.82%
Process-dependent viscoelastic model	$\mu_{v1} = 7.086 \times 10^{4}$ Pa, $\dot{\gamma}_{01} = 4.604 \times 10^{-1}$ s^{-1} $c_{01} = -7.986 \times 10^{-10}$, $m_{01} = 2.296$, $g_{v1} = 1.270 \times 10^{-1}$ $\mu_{v2} = 2.062 \times 10^{5}$ Pa, $\dot{\gamma}_{02} = 1.780 \times 10^{4}$ s^{-1} $c_{02} = -1.337 \times 10^{-1}$, $m_{02} = 3.453$, $g_{v2} = 5.332 \times 10^{-1}$	0.997/1.10%
Classical Maxwell viscoelastic model	$\mu_{v1} = 2.125 \times 10^{4}$ Pa, $\dot{\gamma}_{01} = 1.559 \times 10^{-2}$ s^{-1}, $g_{v1} = 2.838 \times 10^{-1}$ $\mu_{v2} = 1.277 \times 10^{5}$ Pa, $\dot{\gamma}_{02} = 2.328$ s^{-1}, $g_{v2} = 2.896$ $\mu_{v3} = 4.290 \times 10^{4}$ Pa, $\dot{\gamma}_{03} = 1.482 \times 10^{-1}$ s^{-1}, $g_{v3} = 2.269 \times 10^{-1}$ $\mu_{v4} = 1.847 \times 10^{4}$ Pa, $\dot{\gamma}_{04} = 9.284 \times 10^{-4}$ s^{-1}, $g_{v4} = 1.834$	0.969/3.17%

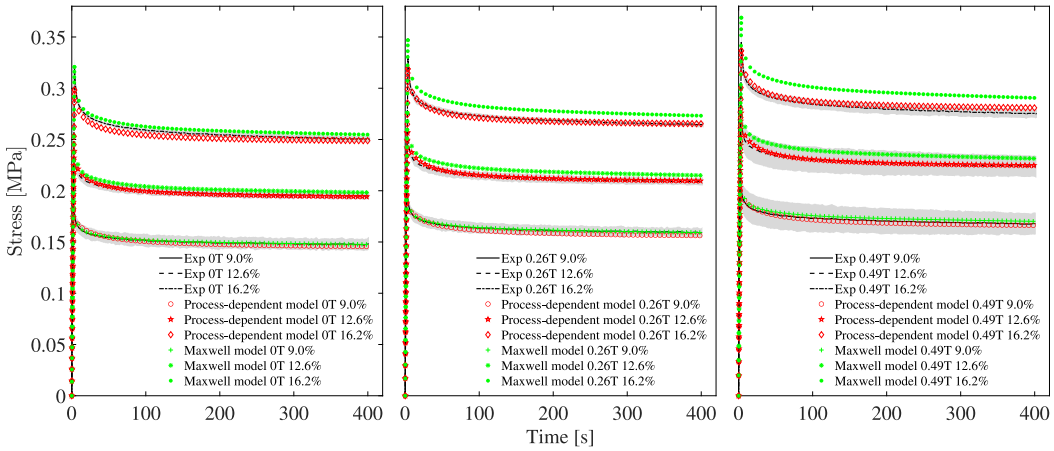

Fig. 12. Comparison of the experimental (Exp) and simulation results of stress relaxation results under different magnetic fields (0, 0.26 and 0.49 T) and strain amplitudes (9.0, 12.6 and 16.2%) by the Process-dependent viscoelastic model and the classical Maxwell model, where experimental scatter is shown in the light-coloured regions.

Subsequently, a new constitutive model incorporating the magnetic-dependent Mullins effect, residual strain and nonlinear viscoelastic behaviour of the isotropic s-MRE is proposed. After parameter identification, it is found that the model fitting result captures the observed magnetic-dependent Mullins effect, residual strain and nonlinear viscoelastic behaviour of the isotropic s-MRE with accuracy. Moreover, to verify that the model can predict the Mullins effect, residual strain and nonlinear viscoelastic in a coupled manner, three cycles of triangular strain with a consecutively increasing strain amplitude under a fast loading rate are conducted for the sample. The comparison between the model prediction and test result is shown to be quite reasonable. In addition, to verify the predictive ability of the model for viscoelastic behaviour at different frequencies, tests and model validation with sinusoidal wave loading are carried out. Validation results show that the proposed model provides reasonable results. To summarize, with the developed model, the magnetic-dependent inelastic behaviours of the isotropic s-MRE can be predicted with accuracy, which is of great benefit for the design of MRE-based smart devices or structures.

Based on the model developed in this work, much research can be pursued in the future. For example, the current model can be implemented into commercial finite element software, such as in ABAQUS® (ABAQUS Version 6.14, Dassault Systémes SIMULIA Corp, United States), to evaluate the magnetic-dependent inelastic performance of the MRE-based devices. Furthermore, since a larger magnetic-dependence of the stress response is exhibited for the anisotropic s-MRE, extending the current model to an anisotropic case is also one of the possible future research directions.

Declaration of competing interest

The authors declare that they have no known competing financial interests or personal relationships that could have appeared to influence the work reported in this paper.

Data availability

Data will be made available on request.

Acknowledgements

The authors thank the financial support from the National Natural Science Foundation of China (12132016, 12202434, 52321003), the Anhui Key R&D Program of China (202104a5020009) and the Fellowship of China Postdoctoral Science Foundation (2022M713045).

Appendix. Numerical implementation algorithm for the nonlinear viscoelastic model

The constitutive equations for the nonlinear viscoelastic model are

$$\begin{cases} -\frac{1}{2}\dot{\overline{\mathbf{F}\mathbf{C}^{v-1}}}\overline{\mathbf{F}}^{\mathrm{T}}\overline{\mathbf{b}}^{e-1} = \dot{\gamma}\dfrac{\mathrm{dev}\left(\overline{\mathbf{b}}^{e}\right)}{\left\|\mathrm{dev}\left(\overline{\mathbf{b}}^{e}\right)\right\|} \\ \dot{\gamma} = \dot{\gamma}_0\left[\sqrt{\dfrac{\overline{I}_1^{v}}{3}} - 1\right]^{c}\left(\dfrac{\left\|\mathrm{dev}\left(\overline{\mathbf{b}}^{e}\right)\right\|}{\sqrt{2}}\right)^{m} \end{cases} . \tag{A.1}$$

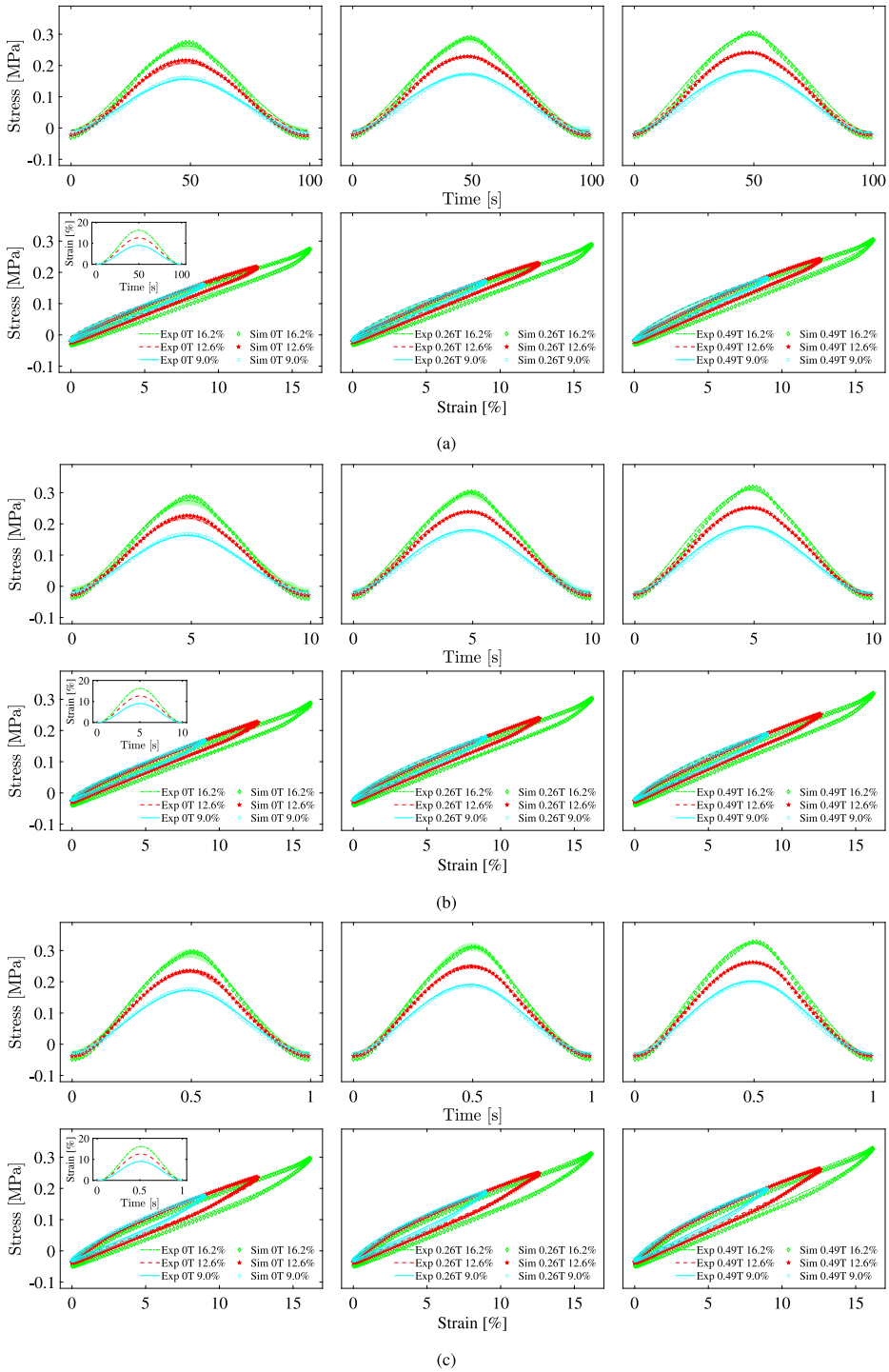

Fig. 13. Experimental (Exp) and simulation (Sim) results of sinusoidal loading with varying magnetic fields and strain amplitudes at different loading frequencies: (a) 0.01 Hz, (b) 0.1 Hz and (c) 1 Hz, where experimental scatter is shown in the light-coloured regions of the stress-time curves.

To solve Eq. (A.1), the operator splitting method (e.g., Reese and Govindjee (1998) and Kaliske (2009)) is applied. Normally, the implementation process consists of two stages: elastic trial and inelastic correction. The specific solution is illustrated by taking a typical time interval $(t_n,\ t_{n+1})$ as an example. The values of the variables at t_n are known. Firstly, during the elastic trial step, the value of $\overline{\mathbf{C}}^{v^{-1}}$ is frozen, therefore,

$$\overline{\mathbf{C}}^{v^{-1}}_{\text{int}} = \overline{\mathbf{C}}^{v^{-1}}_{t_n}, \quad \overline{\mathbf{b}}^{e}_{\text{int}} = \overline{\mathbf{F}}_{t_{n+1}}\,\overline{\mathbf{C}}^{v^{-1}}_{t_n}\,\overline{\mathbf{F}}^{T}_{t_{n+1}}, \tag{A.2}$$

where $(\bullet)_{t_n}$ and $(\bullet)_{t_{n+1}}$ represent the variables at the previous and current time step, respectively. $(\bullet)_{\text{int}}$ denotes the variable obtained through the calculation of the elastic trial process. Afterwards, in the inelastic correction step, there is no change in the deformation gradient. Hence, $\dot{\overline{\mathbf{F}}}^{-1} = \mathbf{0}$ and

$$\dot{\overline{\mathbf{F}}}\dot{\overline{\mathbf{C}}}^{v^{-1}}\overline{\mathbf{F}}^{T} = \dot{\overline{\mathbf{b}}}^{e} - \dot{\overline{\mathbf{F}}}^{-1}\overline{\mathbf{b}}^{e} - \overline{\mathbf{b}}^{e}\overline{\mathbf{F}}^{-T}\dot{\overline{\mathbf{F}}}^{T} = \dot{\overline{\mathbf{b}}}^{e}. \tag{A.3}$$

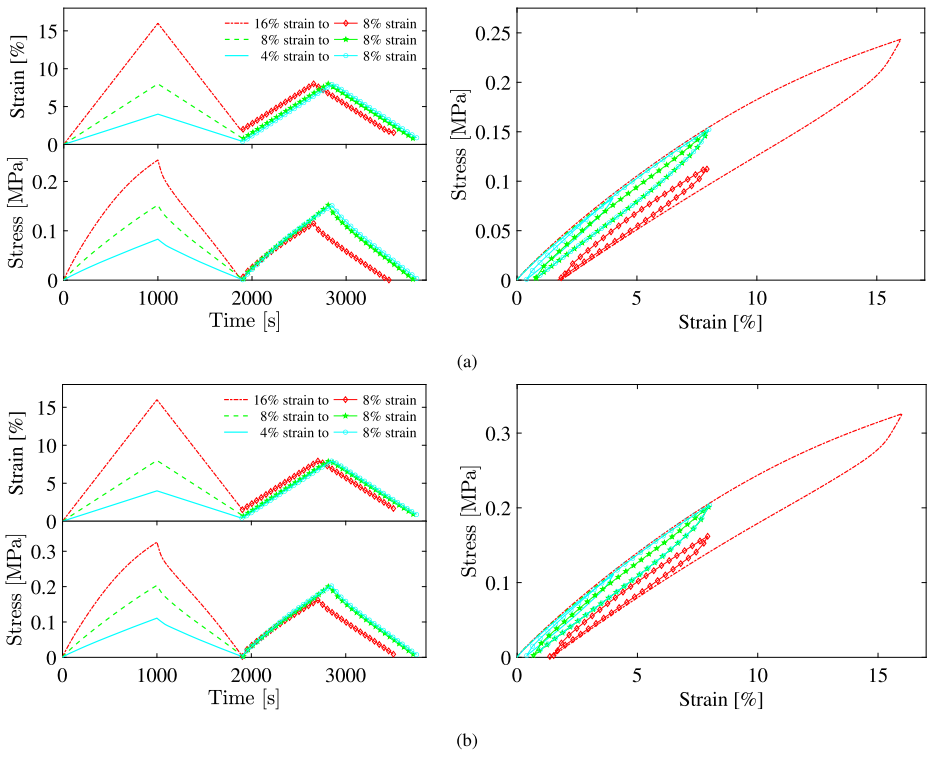

Fig. 14. Prediction results of cyclic loading with varying strain amplitudes at different magnetic fields: (a) 0 T, (b) 1 T.

Inserting Eq. (A.1) into Eq. (A.3), one obtains

$$\dot{\overline{\mathbf{b}}}^{\mathrm{e}} = -2\dot{\gamma}\frac{\operatorname{dev}\left(\overline{\mathbf{b}}^{\mathrm{e}}\right)}{\left\|\operatorname{dev}\left(\overline{\mathbf{b}}^{\mathrm{e}}\right)\right\|}\overline{\mathbf{b}}^{\mathrm{e}}. \tag{A.4}$$

The equation in Eq. (A.4) can be solved by the exponential mapping method (e.g., Kaliske (2009)). Specifically,

$$\overline{\mathbf{b}}^{\mathrm{e}} = \operatorname{expm}\left[-2\int_{t_n}^{t_{n+1}}\dot{\gamma}\frac{\operatorname{dev}\left(\overline{\mathbf{b}}^{\mathrm{e}}\right)}{\left\|\operatorname{dev}\left(\overline{\mathbf{b}}^{\mathrm{e}}\right)\right\|}\mathrm{d}t\right]\overline{\mathbf{b}}^{\mathrm{e}}_{\mathrm{int}}. \tag{A.5}$$

Approximating Eq. (A.5), one obtains

$$\overline{\mathbf{b}}^{\mathrm{e}} \approx \operatorname{expm}\left[-2\dot{\gamma}\frac{\operatorname{dev}\left(\overline{\mathbf{b}}^{\mathrm{e}}\right)}{\left\|\operatorname{dev}\left(\overline{\mathbf{b}}^{\mathrm{e}}\right)\right\|}\Delta t\right]\overline{\mathbf{b}}^{\mathrm{e}}_{\mathrm{int}}, \tag{A.6}$$

where $\Delta t = t_{\mathrm{n}+1} - t_{\mathrm{n}}$. By Eq. (A.6), it is found that $\overline{\mathbf{b}}^{\mathrm{e}}_{\mathrm{int}}$ commutes with $\overline{\mathbf{b}}^{\mathrm{e}}$ and $\operatorname{dev}\left(\overline{\mathbf{b}}^{\mathrm{e}}\right)$. By eigen decomposition, $\overline{\mathbf{b}}^{\mathrm{e}}$ can be expressed as

$$\overline{\mathbf{b}}^{\mathrm{e}} = \sum_{a=1}^{3}\lambda_a^{\mathrm{e}^2}\mathbf{n}_a \otimes \mathbf{n}_a, \tag{A.7}$$

where $\lambda_a^{\mathrm{e}^2}$ and $\mathbf{n}_a$ are the corresponding eigenvalue and eigenvector of $\overline{\mathbf{b}}^{\mathrm{e}}$. By Eqs. (A.7), (A.6) can be rewritten as

$$\lambda_a^{\mathrm{e}} \approx \exp\left\{-\dot{\gamma}\frac{\left[\operatorname{dev}\left(\overline{\mathbf{b}}^{\mathrm{e}}\right)\right]_a}{\left\|\operatorname{dev}\left(\overline{\mathbf{b}}^{\mathrm{e}}\right)\right\|}\Delta t\right\}\lambda_a^{\mathrm{e,int}}, \tag{A.8}$$

where $\left[\operatorname{dev}\left(\overline{\mathbf{b}}^{\mathrm{e}}\right)\right]_a$ is the ath principal stretch of $\left[\operatorname{dev}\left(\overline{\mathbf{b}}^{\mathrm{e}}\right)\right]$ in the form

$$\left[\operatorname{dev}\left(\overline{\mathbf{b}}^{\mathrm{e}}\right)\right]_a = \lambda_a^{\mathrm{e}^2} - \frac{1}{3}\operatorname{tr}\left(\overline{\mathbf{b}}^{\mathrm{e}}\right). \tag{A.9}$$

Introducing $\varepsilon_a^{\mathrm{e}} = \ln\lambda_a^{\mathrm{e}}$ (e.g., Kaliske (2009)), and taking the logarithm of Eq. (A.8) yields

$$\varepsilon_a^{\mathrm{e}} \approx -\dot{\gamma}\Delta t\frac{\left[\operatorname{dev}\left(\overline{\mathbf{b}}^{\mathrm{e}}\right)\right]_a}{\left\|\operatorname{dev}\left(\overline{\mathbf{b}}^{\mathrm{e}}\right)\right\|} + \varepsilon_a^{\mathrm{e,int}}. \tag{A.10}$$

Newton–Raphson method is used to solve Eq. (A.10), and the specific steps are as follows. First, the initial value of the iteration is set to

$$\begin{cases} k = 0, \varepsilon_{a,k}^{\mathrm{e}} = \varepsilon_a^{\mathrm{e,int}} \\ \lambda_{a,k}^{\mathrm{e}} = \exp\left(\varepsilon_{a,k}^{\mathrm{e}}\right) \\ \dot{\gamma}_k = \dot{\gamma}_0\left[\sqrt{\frac{\overline{I}_1^{\mathrm{v}}}{3}} - 1\right]^c\left(\frac{\left\|\operatorname{dev}\left(\overline{\mathbf{b}}_k^{\mathrm{e}}\right)\right\|}{\sqrt{2}}\right)^m \\ r_a = \varepsilon_{a,k}^{\mathrm{e}} + \frac{\dot{\gamma}_k\Delta t\left[\operatorname{dev}\left(\overline{\mathbf{b}}^{\mathrm{e}}\right)\right]_{a,k}}{\left\|\operatorname{dev}\left(\overline{\mathbf{b}}^{\mathrm{e}}\right)\right\|_k} - \varepsilon_a^{\mathrm{e,int}} \end{cases}. \tag{A.11}$$

Afterwards, the calculated residual $\mathbf{r}$ is checked and if $\|\mathbf{r}\| \le \mathtt{tol}$,

$$\begin{cases} \overline{\mathbf{b}}_{t_{n+1}}^{\mathrm{e}} = \overline{\mathbf{b}}_k^{\mathrm{e}} \\ \overline{\mathbf{C}}_{t_{n+1}}^{\mathrm{v}} = \overline{\mathbf{F}}_{t_{n+1}}^{\mathrm{T}}\overline{\mathbf{b}}_{t_{n+1}}^{\mathrm{e}^{-1}}\overline{\mathbf{F}}_{t_{n+1}} \end{cases}. \tag{A.12}$$

Otherwise, an updating is performed for the elastic trial strain $\varepsilon_a^{\mathrm{e}}$ until $\|\mathbf{r}\| \leq \mathtt{tol}$ is satisfied. The corresponding algorithm is

$$
\begin{cases}
K_{ab} = \left.\dfrac{\partial r_a}{\partial \varepsilon_b^{\mathrm{e}}}\right|_{\varepsilon_b^{\mathrm{e}}=\varepsilon_{b,k}^{\mathrm{e}}} \\
\quad = \delta_{ab} + \dfrac{2\Delta t\dot{\gamma}_0}{\left(\sqrt{2}\right)^m}\left(\sqrt{\dfrac{\overline{I}_1^{\mathrm{v}}}{3}}-1\right)^c\left[\left\|\mathrm{dev}\left(\overline{\mathbf{b}}^{\mathrm{e}}\right)\right\|\right]^{m-1}\left(\delta_{ab}-\dfrac{1}{3}\right)\lambda_b^2 \\
\quad + \dfrac{\Delta t\dot{\gamma}_0}{\left(\sqrt{2}\right)^m}\left(\sqrt{\dfrac{\overline{I}_1^{\mathrm{v}}}{3}}-1\right)^c(m-1)\left[\left\|\mathrm{dev}\left(\overline{\mathbf{b}}^{\mathrm{e}}\right)\right\|\right]^{m-3} \\
\quad \times\left[\lambda_a^2-\dfrac{1}{3}\mathrm{tr}\left(\overline{\mathbf{b}}^{\mathrm{e}}\right)\right]\left[\lambda_b^2-\dfrac{1}{3}\mathrm{tr}\left(\overline{\mathbf{b}}^{\mathrm{e}}\right)\right]\lambda_b^2 \qquad ,(a,b\in[1,2,3]). \\
\Delta\varepsilon_b^{\mathrm{e}} = -\left(\boldsymbol{K}^{-1}\right)_{ba} r_a\big|_{\varepsilon_b^{\mathrm{e}}=\varepsilon_{b,k}^{\mathrm{e}}} \\
\varepsilon_{a,k+1}^{\mathrm{e}} = \varepsilon_{a,k}^{\mathrm{e}} + \Delta\varepsilon_b^{\mathrm{e}} \\
\lambda_{a,k+1}^{\mathrm{e}} = \exp\left(\varepsilon_{a,k+1}^{\mathrm{e}}\right) \\
\dot{\gamma}_{k+1} = \dot{\gamma}_0\left[\sqrt{\dfrac{\overline{I}_1^{\mathrm{v}}}{3}}-1\right]^c\left(\dfrac{\left\|\mathrm{dev}\left(\overline{\mathbf{b}}_{k+1}^{\mathrm{e}}\right)\right\|}{\sqrt{2}}\right)^m \\
r_a = \varepsilon_{a,k+1}^{\mathrm{e}} + \dfrac{\dot{\gamma}_{k+1}\Delta t\left[\mathrm{dev}\left(\overline{\mathbf{b}}^{\mathrm{e}}\right)\right]_{a,k+1}}{\left[\left\|\mathrm{dev}\left(\overline{\mathbf{b}}^{\mathrm{e}}\right)\right\|\right]_{k+1}} - \varepsilon_a^{\mathrm{e,int}}
\end{cases}
\tag{A.13}
$$

After the iteration is completed, $\overline{\mathbf{b}}^{\mathrm{e}}{}_{t_{\mathrm{n+1}}}$ and $\overline{\mathbf{C}}^{\mathrm{v}}{}_{t_{\mathrm{n+1}}}$ is obtained by

$$
\begin{cases}
\overline{\mathbf{b}}^{\mathrm{e}}_{t_{\mathrm{n+1}}} = \overline{\mathbf{b}}^{\mathrm{e}}_{k+1} \\
\overline{\mathbf{C}}^{\mathrm{v}}_{t_{\mathrm{n+1}}} = \overline{\mathbf{F}}^{\mathrm{T}}_{t_{\mathrm{n+1}}}\,\overline{\mathbf{b}}^{\mathrm{e}^{-1}}_{t_{\mathrm{n+1}}}\,\overline{\mathbf{F}}_{t_{\mathrm{n+1}}}
\end{cases}
\tag{A.14}
$$

Finally, the numerical solution of viscoelastic stress $\boldsymbol{\sigma}^{\mathrm{mve}}$ is obtained by Eq. (68).

References

Abramchuk, S., Kramarenko, E., Stepanov, G., Nikitin, L.V., Filipcsei, G., Khokhlov, A.R., Zrínyi, M., 2007. Novel highly elastic magnetic materials for dampers and seals: Part i. preparation and characterization of the elastic materials. Polym. Adv. Technol. 18, 883–890.

Amin, A.F.M.S., Lion, A., Sekita, S., Okui, Y., 2006. Nonlinear dependence of viscosity in modeling the rate-dependent response of natural and high damping rubbers in compression and shear: Experimental identification and numerical verification. Int. J. Plast. 22, 1610–1657.

Bastola, A.K., Hossain, M., 2020. A review on magneto-mechanical characterizations of magnetorheological elastomers. Compos. Part B Eng. 200, 108348.

Bergström, J.S., Boyce, M.C., 1998. Constitutive modeling of the large strain time-dependent behavior of elastomers. J. Mech. Phys. Solids 46, 931–954.

Blom, P., Kari, L., 2005. Amplitude and frequency dependence of magneto-sensitive rubber in a wide frequency range. Polym. Test. 24, 656–662.

Brown, W.F., 1966. Magnetoelastic Interactions. Springer Tracts in Natural Philosophy.

Bustamante, R., 2010. Transversely isotropic nonlinear magneto-active elastomers. Acta Mech. 210, 183–214.

Chen, Z., Sun, S., Deng, L., Yang, J., Zhang, S., Du, H., Li, W., 2022. Investigation of a new metamaterial magnetorheological elastomer isolator with tunable vibration bandgaps. Mech. Syst. Signal Process. 170, 108806.

Diani, J., Fayolle, B., Gilormini, P., 2009. A review on the mullins effect. Eur. Polym. J. 45, 601–612.

Dorfmann, A., Ogden, R.W., 2004. A constitutive model for the mullins effect with permanent set in particle-reinforced rubber. Int. J. Solids Struct. 41, 1855–1878.

Dorfmann, L., Ogden, R.W., 2014. Nonlinear Theory of Electroelastic and Magnetoelastic Interacti, Vol. 1. Springer.

Fazekas, B., Goda, T.J., 2021. Constitutive modelling of rubbers: Mullins effect, residual strain, time–temperature dependence. Int. J. Mech. Sci. 210, 106735.

Fu, J., Liao, G., Yu, M., Li, P., Lai, J., 2016. Narx neural network modeling and robustness analysis of magnetorheological elastomer isolator. Smart Mater. Struct. 25, 125019.

Galipeau, E., Castaneda, P.P., 2013. A finite-strain constitutive model for magnetorheological elastomers: Magnetic torques and fiber rotations. J. Mech. Phys. Solids 61, 1065–1090.

Gao, P., Li, H.C., Liu, H., Xiang, C.L., 2021. An innovative torsional vibration absorber of vehicle powertrain system: Prototype design, performance test, and control experiment. Mech. Based Des. Struct. Mach. 1–33.

Govindjee, S., Simo, J., 1991. A micro-mechanically based continuum damage model for carbon black-filled rubbers incorporating mullins' effect. J. Mech. Phys. Solids 39, 87–112.

Haldar, K., 2021. Constitutive modeling of magneto-viscoelastic polymers, demagnetization correction, and field-induced poynting effect. Internat. J. Engrg. Sci. 165, 103488.

Haldar, K., Kiefer, B., Menzel, A., 2016. Finte element simulation of rate-dependent magneto-active polymer response. Smart Mater. Struct. 25, 104003.

Harwood, J., Mullins, L., Payne, A.R., 1965. Stress softening in natural rubber vulcanizates, part ii. stress softening effects in pure gum and filler loaded rubbers. J. Appl. Polym. Sci. 9, 3011–3021.

Hoefer, P., Lion, A., 2009. Modelling of frequency- and amplitude-dependent material properties of filler-reinforced rubber. J. Mech. Phys. Solids 57, 500–520.

Hong, S., Um, Y., Park, J., Park, H.W., 2022. Agile and versatile climbing on ferromagnetic surfaces with a quadrupedal robot. Sci. robot. 7, eadd1017.

Hooshiar, A., Payami, A., Dargahi, J., Najarian, S., 2021. Magnetostriction-based force feedback for robot-assisted cardiovascular surgery using smart magnetorheological elastomers. Mech. Syst. Signal Process. 161, 107918.

Jolly, M.R., Carlson, J.D., Muoz, B.C., 1996. A model of the behaviour of magnetorheological materials. Smart Mater. Struct. 5, 607–614.

Kaliske, H.D., 2009. Bergström-boyce model for nonlinear finite rubber viscoelasticity: theoretical aspects and algorithmic treatment for the fe method. Comput. Mech. 44, 809–823.

Kilian, H.G., Strauss, M., Hamm, W., 1994. Universal properties in filler-loaded rubbers. Rubber Chem. Technol. 67, 1–16.

Landauer, A.K., Li, X., Franck, C., Henann, D.L., 2019. Experimental characterization and hyperelastic constitutive modeling of open-cell elastomeric foams. J. Mech. Phys. Solids 133, 103701.1–103701.26.

Lefèvre, V., Danas, K., Lopez-Pamies, O., 2017. A general result for the magnetoelastic response of isotropic suspensions of iron and ferrofluid particles in rubber, with applications to spherical and cylindrical specimens. J. Mech. Phys. Solids 107, 343–364.

Lejon, J., Kari, L., 2013. Measurements on the temperature, dynamic strain amplitude and magnetic field strength dependence of the dynamic shear modulus of magnetosensitive elastomers in a wide frequency range. J. Vib. Acoust. 135, 064506.

Li, X.Q., Tao, J.L., Landauer, A.K., Franck, C., Henann, D.L., 2022. Large-deformation constitutive modeling of viscoelastic foams: Application to a closed-cell foam material. J. Mech. Phys. Solids 161, 104807.

Li, Q., Yang, X.X., 2014. Experimental study of mechanical properties of N330 carbon black reinforced natural rubber. J. Exp. Mech. 20, 42–50.

Lin, D.Z., Yang, F., Gong, D., Li, R.H., 2023. A new vibration isolator integrating tunable stiffness-damping and active driving properties based on radial-chains magnetorheological elastomer. Mech. Syst. Signal Process. 183, 109633.

Lubliner, J., 1985. A model of rubber viscoelasticity. Mech. Res. Commun. 12, 93–99.

Lucarini, S., Moreno-Mateos, M.A., Danas, K., Garcia-Gonzalez, D., 2022a. Insights into the viscohyperelastic response of soft magnetorheological elastomers: Competition of macrostructural versus microstructural players. Int. J. Solids Struct. 256, 111981.

Lucarini, S., Moreno-Mateos, M., Danas, K., Garcia-Gonzalez, D., 2022b. Insights into the viscohyperelastic response of soft magnetorheological elastomers: Competition of macrostructural versus microstructural players. Int. J. Solids Struct. 256, 111981.

Marckmann, A.G., Verron, A.E., Gornet, A.L., Chagnon, A.G., Charrier, B.P., Fort, B.P., 2002. A theory of network alteration for the mullins effect. J. Mech. Phys. Solids 50, 2011–2028.

Moreno, M.A., Gonzalez-Rico, J., Lopez-Donaire, M.L., Arias, A., Garcia-Gonzalez, D., 2021. New experimental insights into magneto-mechanical rate dependences of magnetorheological elastomers. Composites B 224, 109148.

Moreno-Mateos, M.A., Gonzalez-Rico, J., Nunez-Sardinha, E., Gomez-Cruz, C., Lopez-Donaire, M.L., Lucarini, S., Arias, A., Munoz-Barrutia, A., Velasco, D., Garcia-Gonzalez, D., 2022. Magneto-mechanical system to reproduce and quantify complex strain patterns in biological materials. Appl. Mater. Today 27, 101437.

Mukherjee, D., Bodelot, L., Danas, K., 2020. Microstructurally-guided explicit continuum models for isotropic magnetorheological elastomers with iron particles. Int. J. Non-Linear Mech. 120, 103380.

Nam, T.H., Petríková, I., Marvalová, B., 2021. Experimental and numerical research of stress relaxation behavior of magnetorheological elastomer. Polym. Test. 93, 106886.

Nam, T.H., Petríková, I., Marvalová, B., 2022. Stress relaxation behavior of isotropic and anisotropic magnetorheological elastomers. Contin. Mech. Thermodyn..

Nguyen, T.D., Jones, R.E., Boyce, B.L., 2007. Modeling the anisotropic finite-deformation viscoelastic behavior of soft fiber-reinforced tissues. In: Asme Summer Bioengineering Conference, Vol. 44. pp. 8366–8389.

Norouzi, M., Alehashem, S.M.S., Vatandoost, H., Ni, Y.Q., Shahmardan, M.M., 2016. A new approach for modeling of magnetorheological elastomers. J. Intell. Mater. Syst. Struct. 27, 1121–1135.

Ogden, R.W., Roxburgh, D.G., 1999. A pseudoỳcelastic model for the mullins effect in filled rubber. Proc. R. Soc. Math. Phys. Eng. Sci. 455, 2861–2877.

Psarra, E., Bodelot, L., Danas, K., 2017. Two-field surface pattern control via marginally stable magnetorheological elastomers. Soft Matter 13, 6576–6584.

Psarra, E., Bodelot, L., Danas, K., 2019. Wrinkling to crinkling transitions and curvature localization in a magnetoelastic film bonded to a non-magnetic substrate. J. Mech. Phys. Solids 133, 103734.

Qi, S., Yu, M., Fu, J., Zhu, M., 2017. Stress relaxation behavior of magnetorheological elastomer: Experimental and modeling study. J. Intell. Mater. Syst. Struct. 29, 205–213.

Rambausek, M., Danas, K., 2020. Bifurcation of magnetorheological film–substrate elastomers subjected to biaxial pre-compression and transverse magnetic fields. Int. J. Non-Linear Mech. 128, 103608.

Rambausek, M., Mukherjee, D., Danas, K., 2022. A computational framework for magnetically hard and soft viscoelastic magnetorheological elastomers. Comput. Methods Appl. Mech. Engrg. 391, 114500.

Reese, S., Govindjee, S., 1998. A theory of finite viscoelasticity and numerical aspects. Int. J. Solids Struct. 35, 3455–3482.

Saxena, P., Hossain, M., Steinmann, P., 2013. A theory of finite deformation magneto-viscoelasticity. Int. J. Solids Struct. 50, 3886–3897.

Schubert, G., Harrison, P., 2015. Large-strain behaviour of magneto-rheological elastomers tested under uniaxial compression and tension, and pure shear deformations. Polym. Test. 42, 122–134.

Shariff, M.H.B.M., Bustamante, R., Hossain, M., Steinmann, P., 2017. A novel spectral formulation for transversely isotropic magneto-elasticity. Math. Mech. Solids 22, 1158–1176.

Simo, J.C., 1987. On a fully three-dimensional finite-strain viscoelastic damage model: Formulation and computational aspects. Comput. Methods Appl. Mech. Engrg. 60, 153–173.

Simo, J.C., Hughes, T.J., 2006. Computational inelasticity. Mech. Res. Commun. 7.

Wang, B., Bustamante, R., Kari, L., Pang, H., Gong, X., 2023. Modelling the influence of magnetic fields to the viscoelastic behaviour of soft magnetorheological elastomers under finite strains. Int. J. Plast. 164, 103578.

Wang, B., Kari, L., 2019a. Modeling and vibration control of a smart vibration isolation system based on magneto-sensitive rubber. Smart Mater. Struct. 28, 065026.

Wang, B., Kari, L., 2019b. A nonlinear constitutive model by spring, fractional derivative and modified bounding surface model to represent the amplitude, frequency and the magnetic dependency for magneto-sensitive rubber. J. Sound Vib. 438, 344–352.

Yeoh, O.H., 1993. Some forms of the strain energy function for rubber. Rubber Chem. Technol. 66, 754–771.

Zabihyan, R., Mergheim, J., Pelteret, J.P., Brands, B., Steinmann, P., 2020. FE2 simulations of magnetorheological elastomers: influence of microscopic boundary conditions, microstructures and free space on the macroscopic responses of MREs. Int. J. Solids Struct. 193, 338–356.

Zhu, Y.S., Gong, X.L., Dang, H., Zhang, X.Z., Zhang, P.Q., 2006. Numerical analysis on magnetic-induced shear modulus of magnetorheological elastomers based on multi-chain model. Chin. J. Chem. Phys. 19, 126–130.

Zhu, G.H., Xiong, Y.P., Li, Z.G., Xiao, L., Li, M., Bai, X.X., 2020. A nonlinear dynamic model of magnetorheological elastomers in magnetic fields based on fractional viscoelasticity. J. Intell. Mater. Syst. Struct. 32, 228–239.